

From Equipartition to Curvature: The Spectral Evolution of 4FGL Blazars

MUHAMMAD S. ANJUM,¹ SHU-JIN HOU,¹ LIANG CHEN,² ZHIGANG LI,¹ AND MINFENG GU²

¹*College of Physics and Electronic Engineering, Nanyang Normal University, Nanyang, Henan 473061, China*

²*Shanghai Astronomical Observatory, Chinese Academy of Sciences, 80 Nandan Road, Shanghai 200030, China*

Submitted to ApJS

ABSTRACT

We investigate the evolution of spectral energy distribution (SED) and underlying electron energy distribution (EED) by modeling the nearly simultaneous broadband spectra of selected bright 4FGL blazars, in the context of a combined cooling and stochastic acceleration scenario. We find that one-zone leptonic model with log-parabolic (LP) EED can successfully fit the GeV-TeV emission of blazars. The synchrotron frequency ν_s of blazars mainly evolves due to variation of electron peak energy γ_{3p} . The BL Lac objects (BL Lacs) show a negative trend in the $\nu_s - \nu_s L_s$ SED plane, known as blazar sequence, that does not seem to be an artifact of Doppler boosting, but driven by the equipartition constraints. A positive correlation is found between the derived magnetic field B and electron density n_e , whereas n_e and γ_{3p} negatively relate, as expected in an equipartition scenario. The flat spectrum radio quasars (FSRQs) deviate significantly from such a scenario, indicating their jet parameters should be varying independently. The synchrotron peak frequency ν_s and its spectral curvature b_s negatively correlate for all blazars, confirming the stochastic particle acceleration in blazar jets. However, blazars do not show the signature of hard-sphere acceleration, indicating that magnetic turbulence in the jets might be soft and physical conditions might be near to steady state, consistent with equipartition. Furthermore, for BL Lacs, the SED curvature b_s and the EED curvature r and nearly meet the theoretical relationship $r = 5b_s$, whereas the FSRQs show large deviation due to poor constrain on b_s due to presence of thermal component.

Keywords: Active galactic nuclei (16) — BL Lacertae objects (158) — Blazars (164) — Galaxy jets (601) — Spectral energy distribution (2129)

1. INTRODUCTION

Active galaxies host bright nuclei, called active galactic nuclei (AGN), which shine because of accreting supermassive black holes in the center. Blazars are jetted AGN and their emission is dominated by the nonthermal processes in the relativistic plasma jets moving close to our line of sight. Blazars are marked by broadband emission, extreme variability at high energy, and superluminal motion (R. D. Blandford & M. J. Rees 1978). The orientation of the AGN plane and jet angle with our line of sight play an important role and describe the observed spectral features of several AGN types (C. M. Urry & P. Padovani 1995). Based on the equivalent width of emission lines from fast-moving

clouds in the broad line region (BLR), the blazars can be categorized into flat-spectrum quasars (FSRQs) and BL Lac objects (BL Lacs). However, both classes have similar observed continuum spectra despite their different emission line properties (G. Ghisellini et al. 2011), suggesting similar underlying processes.

The bulk emission of the jet is produced by non-thermal plasma accelerated in the jet via leptonic or hadronic processes (see, e.g., M. Cerruti 2020, for a review on physical processes in the jet). The low-energy hump usually spans radio to X-ray energies and is always associated with leptonic synchrotron emission, whereas the high-energy bump spans from X-rays to very high energy (VHE) γ -rays and, in the leptonic scenario, is attributed to inverse Compton (IC) scattering of low-energy photons by the same electron

population (A. Konigl 1981). In the hadronic scenario, the high energy emission can also arise from a proton synchrotron process (K. Mannheim 1993; A. Mücke et al. 2003). The variability of blazars is attributed to the time dependence of the physical processes in the jet (A. Mastichiadis & J. G. Kirk 1997). In leptonic models, the high-energy IC emission from the jet can be explained either by the synchrotron self-Compton (SSC) (L. Maraschi et al. 1992; S. D. Bloom & A. P. Marscher 1996) or by the external Compton (EC) mechanism (C. D. Dermer & R. Schlickeiser 1993; M. Sikora et al. 1994). Depending on the location of energy dissipation of the jet from the central black hole, various seed photons can contribute to the observed high energy emission, such as host dust illuminated by the central continuum (M. Błażejowski et al. 2000). The one-zone leptonic models have been successful in reproducing the observed broadband spectral energy distribution (SED) of blazars (see, e.g., G. Ghisellini & F. Tavecchio 2009; G. Ghisellini et al. 2010). Thermal emission can be present at several energies, especially in FSRQs, where the optical-UV emission is usually dominated by thermal emission from a hot thin accretion disk. The synchrotron peak frequency and peak luminosity of the blazar SED are important parameters and are indicators of the physical jet conditions of a source.

The broadband SED of blazars is dominated by nonthermal emission shows two characteristic bumps in the $\nu - \nu F_\nu$ logspace (G. Fossati et al. 1998). The peak frequency of low energy synchrotron bump of blazars varies in a wide range of values. The peak frequency of FSRQs falls in the IR band, whereas the peak frequency BL Lacs may fall from IR to X-ray energies (A. A. Abdo et al. 2010). Based on synchrotron peak frequency, blazars can be classified into three classes; low synchrotron peak (LSP), intermediate synchrotron peak (ISP), and high synchrotron peak (HSP) (E. Nieppola et al. 2006; J. H. Fan et al. 2016; J. H. Yang et al. 2022). The BL Lacs can vary from low-to high-peak sources, whereas almost all FSRQs are practically low-peak sources. Blazars generally show an inverse correlation between synchrotron peak frequency and luminosity or radiation power, a trend known as blazar sequence (G. Fossati et al. 1998). This observed sequence was explained in terms of radiative cooling scenario in which jet power derives the anti-correlation (G. Ghisellini et al. 1998; G. Ghisellini & F. Tavecchio 2008), but criticized as a selection effect (P. Giommi et al. 2012) or an observational feature due to Doppler boosting (E. Nieppola et al. 2008; J. H. Fan et al. 2017).

Blazar SEDs are curved and can be fitted by a higher-order polynomial or log-parabolic (LP) function. E. Massaro et al. (2004) found that even in a small energy band, the spectra are significantly curved, suggesting that the source electron energy distribution (EED) must be mildly curved, rather than a power law. Although astrophysical acceleration mechanisms usually produce a power-law EED, the energy dependence of acceleration probability (E. Massaro et al. 2004) or a random fluctuations of fractional gain in the underlying acceleration mechanisms can produce a LP EED (A. Tramacere et al. 2011). Furthermore, in such an acceleration mechanism, the synchrotron peak frequency ν_s and the synchrotron spectral curvature b_s anti-correlate. Previously it has been found that the peak frequency and curvature parameter are indeed anti-correlated (see, for example A. Tramacere et al. 2007; L. Chen 2014). However, the slope is different for various blazar types (J. H. Fan et al. 2016). The imprint of this correlation on the emitting EED, i.e., a correlation between EED peak energy and its curvature has not been widely studied and requires the modeling of simultaneous broadband SEDs of a large blazar sample.

The spectral evolution of blazar SED is an important but complex topic since the emission and acceleration models have a large number of parameters. It is not clear which parameters drive the spectral behavior of blazars in the rest-frame νL_ν SED. Even the SED of a single source is highly variable over time, and the true origin of the variability is not fully understood. The spectral changes in the νL_ν SED can arise either due to EED parameters; such as electron energy and density, or ambient conditions such as the energy density of magnetic field and photon fields, or beaming parameters, such as the Doppler factor, or a combination of all. To investigate the genuine origin of the spectral shifts or variability in the blazar SED, it is important to model the SEDs of a large sample of blazars of the same SED class. A statistical trend in the $\nu_s - \nu_s L_s$ plane, with ν_s being the synchrotron peak frequency and $\nu_s L_s$ the peak luminosity, produces a systematic evolution of source parameters and might explain how the parameters are linked. Previously, it has been found that HSP BL Lacs show a positive relationship between the synchrotron frequency and luminosity and a negative one between synchrotron frequency and its spectral curvature, which can be explained in a combined scenario of synchrotron cooling and statistical acceleration (A. Tramacere et al. 2007; F. Massaro et al. 2008; A. Tramacere et al. 2009). However, the observations were limited to X-rays. In this work, we

explore the multiwavelenght behavior of blazars.

We selected a sample of bright Fermi-detected blazars to study the spectral evolution of the blazars in the νL_ν SED and its imprint on the emitting EED. In the first step, we performed LP parametric fitting of the SEDs to find the synchrotron frequency, flux, luminosity, and spectral curvature to study the behavior of observed SEDs. In the next step, we employ a physical one-zone synchrotron+IC model, in the context of a combined cooling and stochastic scenario, to model the blazar SEDs to investigate how changes in SED and EED are related. We, then, study the relationship between the SED observables and the source parameters of one-zone model to investigate the evolution of blazars in $\nu - \nu L_\nu$ plane and how the spectral curvature evolves against synchrotron frequency. We describe the blazar sample in Section 2, the blazar model in Section 3, and our findings and results in Section 4. Section 5 provides a discussion and summarizes our results. Throughout this work, we assume the standard cosmological model with $\Omega_m = 0.32$, $\Omega_\Lambda = 0.68$, and the $H_0 = 70 \text{ km s}^{-1} \text{ Mpc}^{-1}$.

2. SAMPLE & DATA

Spectral fitting and physical modeling of snapshot SEDs of a blazar sample can provide important insights into the emission mechanisms, the origin of their spectral variability, and the evolution of cooling/acceleration processes in the blazar jets. We choose 100 γ -ray blazars from the Fermi-LAT bright AGN sample (LBAS) with sufficient SED data, corrsponding to the first four months of Fermi-LAT operations, from August 2008 to December 2008 (A. A. Abdo et al. 2009). The sample includes about 40 BL Lacs and 60 FSRQs. The broadband SEDs of selected LBAS blazars were compiled by A. A. Abdo et al. (2010), however, the energy range of the first LAT data release (0.1 – 300 GeV) was relatively small to constrain the high energy peak and shape of several blazars, especially the HSP sources. Recently, the third data release of the fourth Fermi-LAT catalog (4FGL-DR3) released the γ -ray data of these blazars in a broad energy range (0.1 GeV to 50 TeV) (M. Ajello et al. 2022). Due to a significantly large energy range, the high-energy peak of blazars can be fully constrained, leading to a more reliable estimate of physical jet parameters. We gathered the spectra data of these 100 4FGL blazars from radio to TeV γ -ray, from the Space Science Data Center (SSDC) of Italian Space Agency (ASI)³ (G. Stratta et al. 2011) to build their broadband

SEDs. We collected the Planck radio data (Planck Collaboration et al. 2011), WISE IR data, optical-UV data from SWIFT-UVOT, 0.1 – 10 keV X-ray data from the SWIFT-XRT point source catalog (1SWXRT, V. D’Elia et al. 2013), and 4FGL-DR3 γ -ray data (S. Abdollahi et al. 2020). From IR to X-rays, we ensure that the spectra data is nearly simultaneous, taken within a few weeks to a few months. Occasionally, when available, we use recently released multiband X-ray data from the eROSITA all-sky survey (A. Merloni et al. 2024) or historical data from BeppoSAX (P. Giommi et al. 2002) to provide better constraints to the model parameters. To account for variability and guide the fitting algorithm, we induce a $\simeq 10\%$ systematic error. Incorporating these data, the LP parametric fitting and physical model fitting can be fully constrained, providing an opportunity to compare models with the observed data, to investigate the spectral changes of blazars in the $\nu_s - \nu_s L_{\nu_s}$ plane.

3. THE ONE-ZONE BLAZAR MODEL

Firstly, we perform the LP polynomial fitting of Blazar SEDs to estimate the SED observables, such as peak frequency, peak flux and luminosity, and the curvature of the synchrotron/IC components. The high-energy spectra of blazars is generally curved and deviates significantly from a power-law (E. Massaro et al. 2004). Recently, Fermi-LAT found several thousands of blazars with log-parabolic spectra (M. Ajello et al. 2022). In a small energy band, the energy spectrum of a blazar shows LP form, given as

$$F(E) = K \left(\frac{E}{E_0} \right)^{-(a+b \log(E/E_0))}, \quad (1)$$

where E_0 is the reference energy. The peak energy E_p of LP spectrum in terms spectral index a and curvature parameter b becomes

$$E_p = E_0 10^{\left(\frac{2-a}{2b}\right)}. \quad (2)$$

The broadband SED roughly matches the LP function and is a reflection of an underlying LP EED. Such a curved EED is naturally produced in an energy-dependent scenario in which the acceleration efficiency decays with particle energy (E. Massaro et al. 2004) or a stochastic acceleration scenario in which the fractional energy gain is purely random. The LP function that describes the broadband blazar SED is given as

$$\log(\nu F_\nu) = \log(\nu_p F_{\nu_p}) - b(\log \nu - \log \nu_p)^2, \quad (3)$$

where ν_p is the peak frequency and b is the curvature of the fitted bump. We fit this polynomial to all

³ <https://www.ssdc.asi.it>

blazar SEDs to determine the peak frequency, flux, and curvature of the synchrotron and IC bumps. The peak luminosity is then found to be $L = 4\pi d_L^2(\nu_p F_{\nu_p})$.

Secondly, at the pre-fitting, we estimate the approximate one-zone model parameters from the SED observables. The spectral parameters of synchrotron/IC bump reflect the physical conditions inside the jet and help estimate the physical parameters of a one-zone model, such as electron peak energy γ_p , ambient magnetic field B , emission source size R , and the Doppler factor δ (see, e.g., G. Ghisellini et al. 1996; F. Tavecchio et al. 1998; L. Chen 2018). For example, the synchrotron peak frequency ν_s relates B and δ as

$$\nu_s = C_0 \gamma_p^2 B' \delta, \quad (4)$$

whereas the SSC peak frequency due to these synchrotron photons becomes

$$\nu_c = \frac{4}{3} \gamma_p'^2 \nu_s. \quad (5)$$

The electron peak energy γ_p can, thus, be approximated from observed frequencies as

$$\gamma_p' \simeq \sqrt{\frac{\nu_c}{\nu_s}}. \quad (6)$$

The magnetic energy density $U'_B = B'^2/8\pi$ and the synchrotron energy density in the jet frame $U'_s \simeq L_s/4\pi R^2 c \delta^4$ can be constrained from the SSC dominance parameter (the ratio of SCC losses to synchrotron loss rates) as

$$\frac{L_c}{L_s} = \frac{U'_s}{U'_B} \simeq \frac{2L_s}{cB'^2 R^2 \delta^4}, \quad (7)$$

relating the magnetic field B' and δ . This equation, together with the expressions for ν_s , leads to the estimation of B and δ as

$$B' \simeq \frac{R \nu_s^4}{C_0^2 \nu_c^2 L_s} \sqrt{\frac{c L_c}{2}} \quad (8)$$

and

$$\delta \simeq \frac{C_0 \nu_c L_s}{\nu_s^2 R} \sqrt{\frac{2}{c L_c}}. \quad (9)$$

For the EC component, various external photon fields might contribute to IC emission, depending on the location of energy dissipation of the jet, such as from the broadband line region (BLR), a dusty torus (DT), or even cosmic microwave background (CMB). Assuming the DT source photons, the EC frequency can be approximated as

$$\nu_c = \frac{4}{3} \gamma_p'^2 \Gamma \nu_T \delta, \quad (10)$$

where ν_T is the frequency of DT seed photons in the AGN frame. The external seed photon energy density in the jet frame becomes

$$U'_{ext} \simeq \frac{17}{12} \Gamma^2 U_T, \quad (11)$$

where U_T is the source photon energy density of the DT field illuminated by the thermal accretion disk, given by

$$U_T = \frac{\eta L_D}{4\pi R_T^2 c}. \quad (12)$$

Here L_D is the central disk luminosity, R_T is the DT radius, and η is the fraction of disk luminosity reprocessed by DT. We assume $\eta = 0.1$, i.e., a 10% of disk luminosity being reprocessed into the jet. Then the EC dominance parameter becomes

$$\frac{L_c}{L_s} = \frac{U'_{ext}}{U'_B} \simeq \frac{2\Gamma^2 L_D}{B'^2 R_T^2 c}. \quad (13)$$

Approximating the jet parameters at the pre-fitting stage, we then use a one-zone model with synchrotron+SSC+EC components to fit the sample SEDs based on the χ^2 minimization algorithm *JetSet* (A. Tramacere 2020). The algorithm optimizes the model fit on the SEDs by varying the parameter values around the approximate values, till the fit is converged.

We assume a one-zone leptonic model with an expanding homogeneous blazar blob of radius R , filled with uniform electron distribution $N(\gamma)$ and chaotic magnetic field B , moving relativistically with speed Γ , making an angle θ with our line of sight. The size of expanding blob R depends on the jet opening angle ϕ and distance of the blob from the central black hole R_b as

$$R = R_b \tan \phi. \quad (14)$$

We assume a line-of-sight angle $\theta \simeq 3$ and an opening angle $\phi \simeq 5$ which are typical of blazars, and the distance of the R_b as a free parameter. The size of the torus R_T scales with source disk luminosity L_D as

$$R_T = 2 \times 10^{18} L_{D,45}^{1/2} \quad (15)$$

where the disk luminosity $L_{D,45}$ is constrained by fitting a blackbody to the BBB, observed at optical-UV SED. The emitting electron distribution is considered to be LP in the energy ranging from γ_{min} to γ_{max} , given as

$$N(\gamma) = N_0 \left(\frac{\gamma}{\gamma_0} \right)^{-s-r \log(\gamma/\gamma_0)} \quad (16)$$

where γ_0 is the reference electron energy, and s and r are the spectral index and curvature at γ_0 . The LP EED

is essentially a broken power law distribution, broken at several energy points, and is naturally produced due to a balance between a stochastic acceleration and radiative cooling (N. S. Kardashev 1962; E. Massaro et al. 2006; K. Katarzyński et al. 2006). The peak energy of LP EED in the $\gamma^3 N(\gamma)$ representation is given by

$$\gamma_{3p} = \gamma_0 10^{\left(\frac{3-s}{2r}\right)}. \quad (17)$$

Thus, the particle energy and curvature are inversely related in stochastic acceleration as

$$\log \gamma_{3p} = \log \gamma_0 + \left(\frac{3-2s}{2r} \right). \quad (18)$$

By one-zone leptonic model fitting of the blazar SEDs assuming LP EED, we derive the physical jet parameters, such as, the magnetic field B , blob radius R , blob location R_b , jet bulk factor Γ , Doppler factor $\delta = [\Gamma(1 - \beta \cos \theta)]^{-1}$, electron density n_e , electron energy γ_0 , and spectral curvature r . The corresponding components of jet power in the galaxy frame as

$$L_i \simeq \pi R^2 c \Gamma^2 U_i, \quad (19)$$

where U_i represents the ambient energy density of the magnetic field U_B , emitting electrons U_e , and cold protons U_p , given as

$$U_B = \frac{B^2}{8\pi} \quad (20)$$

$$U_e = m_e c^2 \int \gamma n_e(\gamma) d\gamma \quad (21)$$

$$U_p = m_p c^2 \int n_p(\gamma) d\gamma. \quad (22)$$

We use the number density of cold protons equal to electrons $n_p = n_e$. The total jet power of a source, then, becomes $L_{jet} = L_e + L_p + L_B$. The radiation power of the jet is estimated as

$$L_{rad} \simeq \frac{L_{bol}}{\Gamma^2} \quad (23)$$

where L_{bol} is the bolometric luminosity. For IC emission using a full Klein-Nishina cross-section, we calculate the SSC emission due to internal synchrotron photons and EC emission due to external photons from a relatively colder DT with temperature $T_T \sim 10^2$ K, illuminated by a hot disk at a temperature $T_D \sim 10^4$ K with luminosity L_D . The disk luminosity L_D is directly constrained by the big blue bump (BBB) in the observed SED, and for sources where the BBB is not observable, we use the optical-UV data as an upper limit. For three nearby HSP BL Lacs (4FGL J1517.7-2422, 4FGL J1653.8+3945, and 2009.4-4849) with $z < 0.1$, we find the signature of background host galaxy in their synchrotron spectra and fit the host galaxy template to account for this emission.

3.1. Combined Cooling and Acceleration Scenario

The synchrotron SED from a LP EED is nearly a log-parabola with peak frequency

$$\log \nu_s \propto \log \gamma_0 + \frac{3}{10b_s}, \quad (24)$$

where b_s is the curvature of synchrotron photon spectra and related to electron curvature parameter r as $r = 5b_s$ (E. Massaro et al. 2006). Thus, modeling the blazar SEDs reveal how the intrinsic electron curvature r evolves in acceleration and cooling conditions. The spectral curvature is an important parameter and reflects the internal conditions of the blazar jet.

We discuss the evolution of LP EED curvature r against its peak energy γ_{3p} in a combined cooling and stochastic acceleration scenario. In stochastic acceleration models, the injected particles get accelerated by interactions with magnetohydrodynamic waves produced by magnetic turbulence and the process is described as diffusive shock acceleration (A. Tramacere et al. 2011). In a combined scenario including all relevant processes, the time evolution of injected electrons is governed by the kinetic equation

$$\frac{\partial N(\gamma, t)}{\partial t} = \frac{\partial}{\partial t} [(C(\gamma, t) - A(\gamma, t)) N(\gamma, t)] + D(\gamma, t) \frac{\partial N(\gamma, t)}{\partial \gamma} - E(\gamma, t) + Q(\gamma, t) \quad (25)$$

where $C(\gamma, t)$ is the cooling parameter, given in terms of ambient energy density in the jet $U_{tot}(\gamma, t)$ as

$$C(\gamma, t) = \frac{4}{3} \frac{\sigma_T c}{m_e c^2} U_{tot}(t), \quad (26)$$

and $A(\gamma, t)$ is the acceleration term defined in terms of diffusion coefficient $D(\gamma, t)$ as

$$A(\gamma, t) = \frac{2}{\gamma} D(\gamma, t). \quad (27)$$

The terms $E(\gamma, t) = N(\gamma, t)/\tau_{esc}$ and $Q(\gamma, t)$ are the escape and injection terms. In a simple acceleration+cooling scenario, the equilibrium energy is determined by competition between acceleration and cooling timescales, i.e., $\tau_c(\gamma) \simeq \tau_a(\gamma)$. The cooling timescale is inversely related to particle energy and ambient energy density in the jet as

$$\tau_c(\gamma) \simeq \frac{mc^2}{\sigma_T c \gamma U_{tot}}, \quad (28)$$

where $U_{tot} = U_B + U_s + U_{ext}$ is the total ambient energy density in the jet, available for radiative cooling

processes. The acceleration timescale of electrons is described by the diffusion coefficient as

$$\tau_a(\gamma) = \frac{\gamma^2}{D(\gamma)} \approx \left(\frac{\gamma}{\gamma_0} \right)^{2-q}, \quad (29)$$

where q is the index of magnetic turbulence spectra $W(k)$ in terms of wave number $k = 2\pi/\lambda$, given as

$$W(k) = \frac{(\delta B)^2}{8\pi} \left(\frac{k}{k_0} \right)^{2-q}. \quad (30)$$

The turbulence index q determines the evolution of EED in the combined scenario. For hard-sphere spectrum $q = 2$, whereas $q < 2$ for the Kolmogorov spectrum or the Kraichnan spectrum. Thus, for a hard-sphere acceleration, the acceleration time becomes independent of particle energy γ .

In diffusive shock acceleration, the fractional energy gain is a random variable and the evolution of EED shows that the curvature r decays with particle energy as long as the acceleration times are shorter than the typical acceleration time (A. Tramacere et al. 2011). Thus, for an acceleration dominated regime ($t < t_a$), the curvature r and peak energy of electrons γ_{3p} must follow an inverse relation

$$r \propto \frac{1}{\gamma_{3p}}. \quad (31)$$

Such an inverse correlation between curvature and particle energy can also be explained if the acceleration probability is energy dependent, such that $p_i \propto 1/\gamma^a$, where a is a constant showing energy dependence (E. Massaro et al. 2004). Although both the stochastic and energy-dependent acceleration mechanisms predict an inverse correlation between peak energy and curvature, the efficiency of both mechanisms could be different. We investigate the impression of stochastic acceleration and radiative cooling mechanisms on the observed blazar SED.

4. MODELING RESULTS

We perform a statistical analysis of spectral parameters blazars, derived by LP polynomial fitting and one-zone model fitting, to investigate the spectral evolution of SED and the source EED in the combined scenario. The peak frequency, flux, luminosity, curvature, and the Compton dominance of BL Lacs and FSRQs, derived through polynomial fitting, are reported in Table 1 and Table 2, respectively. Based on synchrotron peak frequency ν_s , we find that 72 blazars are LSP sources, whereas 28 sources fall into the ISP/HSP category. Then, based on the type of a blazar, we choose the one-zone model with appropriate

model components to fit the broadband SEDs using χ^2 minimization technique. We find that the GeV-TeV γ ray emission of all ISP/HSP blazars (designated as SSC blazars) can be fitted well with the SSC model satisfactorily, as shown in Figure 16; whereas all LSP blazars (designated as EC blazars) necessarily need an additional EC component, as shown in Figure 17. In addition to FSRQs, the EC blazars also include and LSP BL Lacs, as these sources inevitably need the EC component (e.g., H.-B. Hu et al. 2024). The X-ray emission in the EC blazars is produced mainly by the SSC component, whereas the γ -ray emission is dominated by the dusty torus EC component (EC-DT). The physical one-zone model parameters of BL Lacs and FSRQs are shown in Table 3 and Table 4, respectively.

Interestingly, for some highly γ -ray dominant FSRQs with highly steep X-ray spectra (such as J0530.9+1332, J1016.0+0512, J1510.8-0542, J1522.1+3144, J2147.1+0931), the EC-DT component completely dominates the SSC emission, either due to strong ambient photon field or a higher collimation of the jet (M. Sikora 1997). This shows that, for highly luminous and Compton dominated FSRQs, the SSC component might be of secondary importance or practically irrelevant at X-ray energies. For a few sources (such as J0217.8+0144, J0221.1+3556, J0238.6+1637, J0334.2-4008, J1147.0-3812, and 4FGL J2203.4+1725), the EC-DT component under-produces the VHE γ -rays (> 100 GeV). It does not affect our jet parameters estimation since the physical parameters are related to SED peaks, however, it indicates that some blazars might need a significant contribution from BLR photons to account for the high energy tail of Fermi-LAT γ -ray spectra. Our modeling results are consistent with previous studies suggesting that the location of the γ -ray production should be inside the molecular torus, nearly at the edge of the BLR (see, e.g., L. Costamante et al. 2018; S.-J. Kang et al. 2014; H.-B. Hu et al. 2024).

The distributions of physical jet parameters of blazars are shown in Figure 1. The parameter space is similar to previous blazar studies (see, e.g., C. Tan et al. 2020; M. S. Anjum et al. 2020). On average, the FSRQs possess an order of magnitude higher magnetic field ($B \approx 0.1$ G) as compared to BL Lacs ($B \sim 0.01$ G); however, both sources show a similar jet size $R \sim 10^{17}$ cm. The Doppler factor δ for BL Lacs, on average, is higher (> 20) than for FSRQs (< 20). The total ambient energy density U_{tot} for FSRQs is several orders of magnitude higher than BL Lacs due to external DT photon

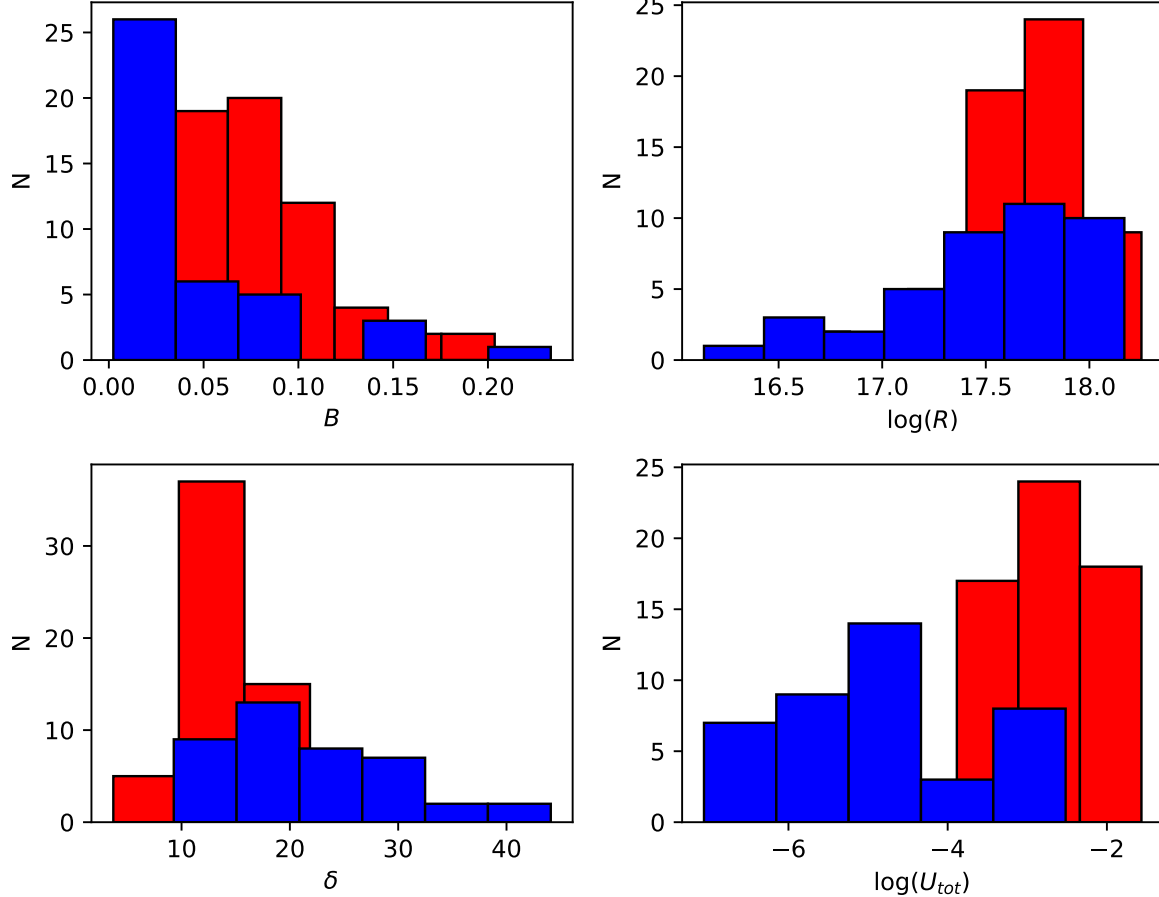


Figure 1. The distributions of physical jet parameters of BL Lacs (blue) and FSRQs (red).

field. Figure 2 shows the source EED parameters of best model fitting. The average spectral index s is higher for FSRQs ($s \approx 2.5$) than for BL Lacs ($s < 2$), however, the curvature parameter r overlap significantly for the two populations. The electron reference energy γ_0 in BL Lacs varies across several orders of magnitude, whereas for FSRQs it varies in a small range (100 – 1000). The total jet power L_{tot} and radiative power L_{rad} of FSRQs dominates the BL Lacs, as shown in Figure 3, indicating a stronger radiative cooling in FSRQs in the context of blazar sequence. The BL Lacs show average total jet power $L_{tot} < 10^{46}$ erg s $^{-1}$, whereas the FSRQs show $L_{tot} > 10^{47}$ erg s $^{-1}$. For FSRQs sources, the disk luminosity L_D varies in the range $10^{44} – 10^{48}$ erg s $^{-1}$ and seems to be positively correlated to the location of the jet blob R_b , that varies from subpc to pc scale, as shown in Figure 4. This suggests that the location of energy dissipation R_b might be related to accretion power (as $L_{acc} \propto \eta L_D$) and, thus, the γ -ray power (as $L_\gamma \propto L_D$). Similar results were found by (D. Yan et al. 2012) who modeled the broadband SEDs of 21 FSRQs.

4.1. Spectral Evolution of Blazars

The LP polynomial function is relatively milder than an exponential law and fits the blazar spectra adequately. Fitting the blazar SEDs can reveal the spectral variations and underlying parameters that produce these variations. Therefore, based on logarithmic parabolic polynomial fitting using Equation 3, we measure the spectral parameters of both synchrotron and IC components and relate these quantities to physical jet parameters derived through the one-zone model fitting. Since the jet properties of the BL Lacs and FSRQs are similar in each class, studying these classes separately makes their spectral behavior more prominent. To measure the spectral parameters, we fit the polynomial+BBB-template on synchrotron bump of LSP sources, whereas a polynomial+host galaxy template for ISP/HSP sources. While almost all FSRQs shows a BBB, only three nearby BL Lacs show the host galaxy emission. As the curvature measurement is sensitive to fitted frequency window, We fitted the polynomial in same frequency window for BL Lacs and

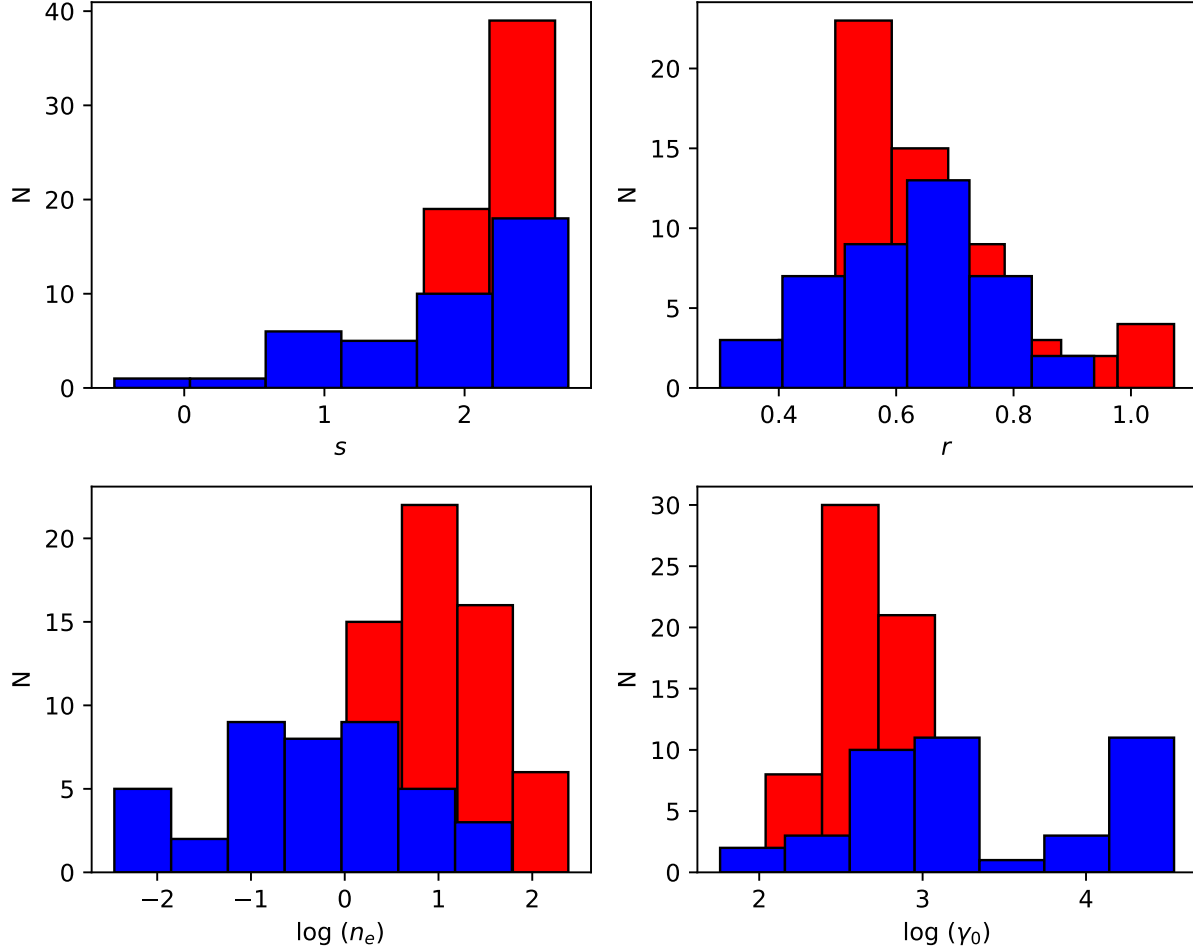


Figure 2. The distributions of source electron energy distribution (EED) parameters for BL Lacs (blue) and FSRQs (red).

FSRQs to eliminate possible systematic biases. Figure 5 shows two representative cases of LP polynomial fitting.

We find that the synchrotron frequency ν_s of both blazar types seems to be positively correlated with synchrotron flux $\nu_s F_s$, however, the Compton frequency ν_c and flux $\nu_c F_c$ do not seem to be related, as shown in Figure 6. This trend is, however, not intrinsic and appear to be an effect of the luminosity distance. The BL Lacs show an inverse relationship in both the $\nu_s - \nu_s L_s$ and $\nu_c - \nu_c L_c$ planes with correlation coefficient $r_p \approx -0.4$ and a chance probability $p \sim 10^{-3}$, as shown in Figure 7. The FSRQs almost show no correlation in these SED planes. Similarly, the peak frequencies ν_s and ν_c are significantly positively correlated related for BL Lacs having best fitting relationship $\log \nu_c = 0.9 \log \nu_s + 10.44$ with $r_p \approx 0.9$ and $p \sim 10^{-16}$, as shown in Figure 8, confirming the the SSC nature of their high energy emission $\nu_c = \gamma_{3p}^2 \nu_s$ (R. X. Zhou

et al. 2021). The FSRQs do not show any relationship between the peak frequencies. These systematic trends observed for BL Lacs only suggest that their spectra might evolve differently from FSRQs.

The anti-correlation between peak frequency ν_s and luminosity $\nu_s L_s$ for BL Lacs is consistent with the blazar sequence. In the blazar sequence, the higher jet power (\propto accretion power) derives the inverse relationship, such that the FSRQs have higher jet power than BL Lacs due to increased ambient density U_{tot} , which limits the electron energy γ_{3p} due to efficient cooling (G. Ghisellini et al. 1998; G. Ghisellini & F. Tavecchio 2008). However, the blazar sequence does not explain the internal relationship between the physical parameters, such as magnetic field B , particle density n_e , and the particle energy γ_{3p} . Moreover, the blazar sequence has been criticized as a selection effect or an artifact of Doppler boosting (E. Nieppola et al. 2008). The systematic trends observed for BL Lacs

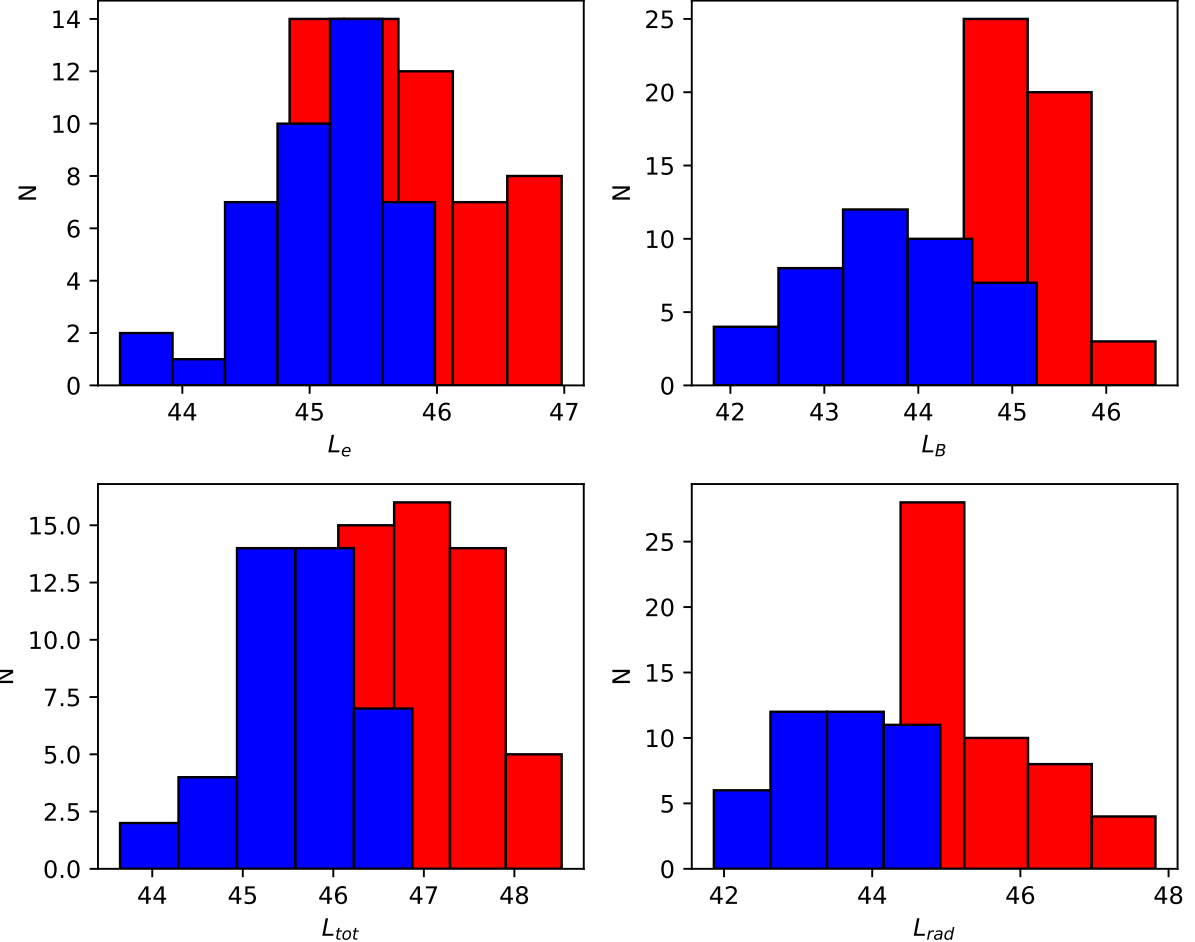


Figure 3. The distributions of jet power for BL Lacs (blue) and FSRQs (red).

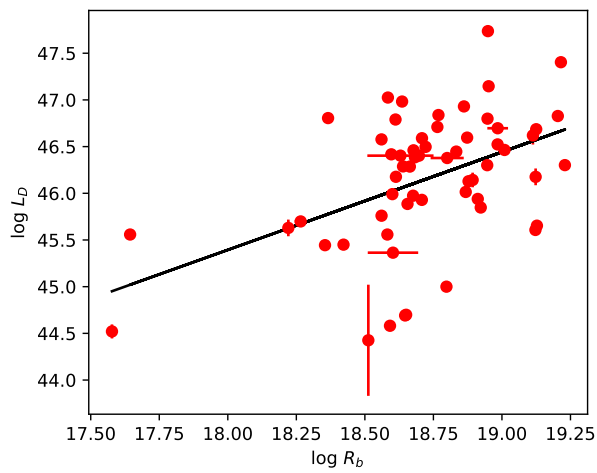


Figure 4. The relationship between dissipation location R_b and the accretion disk luminosity L_D for FSRQs. The solid line shows the best linear regression fit.

in the synchrotron and IC $\nu_p L_p$ SED planes indicate that the jet parameters might be correlated. We, therefore, explore the internal relationship between source parameters that can mimic the blazar sequence.

The observed inverse relationship between ν_s and $\nu_s L_s$ for BL Lacs cannot be dominated by changes in a single jet parameter such as magnetic field B , peak energy γ_{3p} , or Doppler factor δ ; since such changes would rather lead to a positive relationship between ν_s and $\nu_s L_s$, as expected in a pure synchrotron cooling scenario. Assuming a synchrotron scenario with independent jet parameters, the peak frequency and luminosity follow a positive scaling relation $\nu_s L_s \propto \nu_s^\alpha$, where

$$\nu_s \propto \gamma_{3p}^2 B \delta \quad (32)$$

is the synchrotron peak frequency,

$$\nu_s L_s \propto n_e \gamma_{3p}^2 B^2 R^3 \delta^4 \quad (33)$$

is the synchrotron peak luminosity, and α is the slope that indicates the parameters causing the spectral

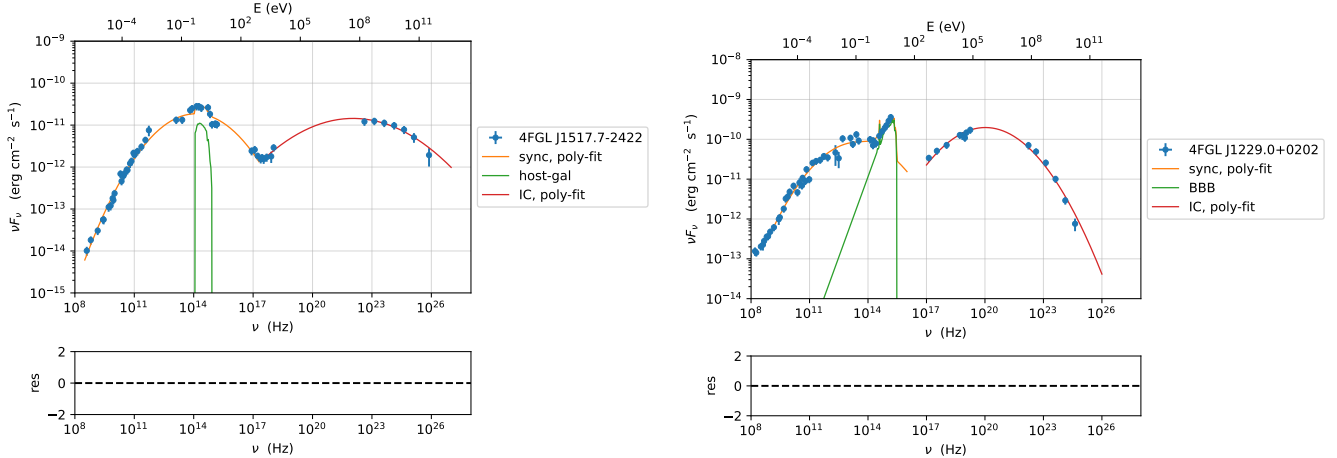


Figure 5. An example of log-parabolic polynomial fitting of blazars. The *left panel* shows the BL Lac source ApLib (4FGL J1517.7-2422), whereas the *right panel* shows the FSRQ 3C273 (4FGL J1229.0+0202).

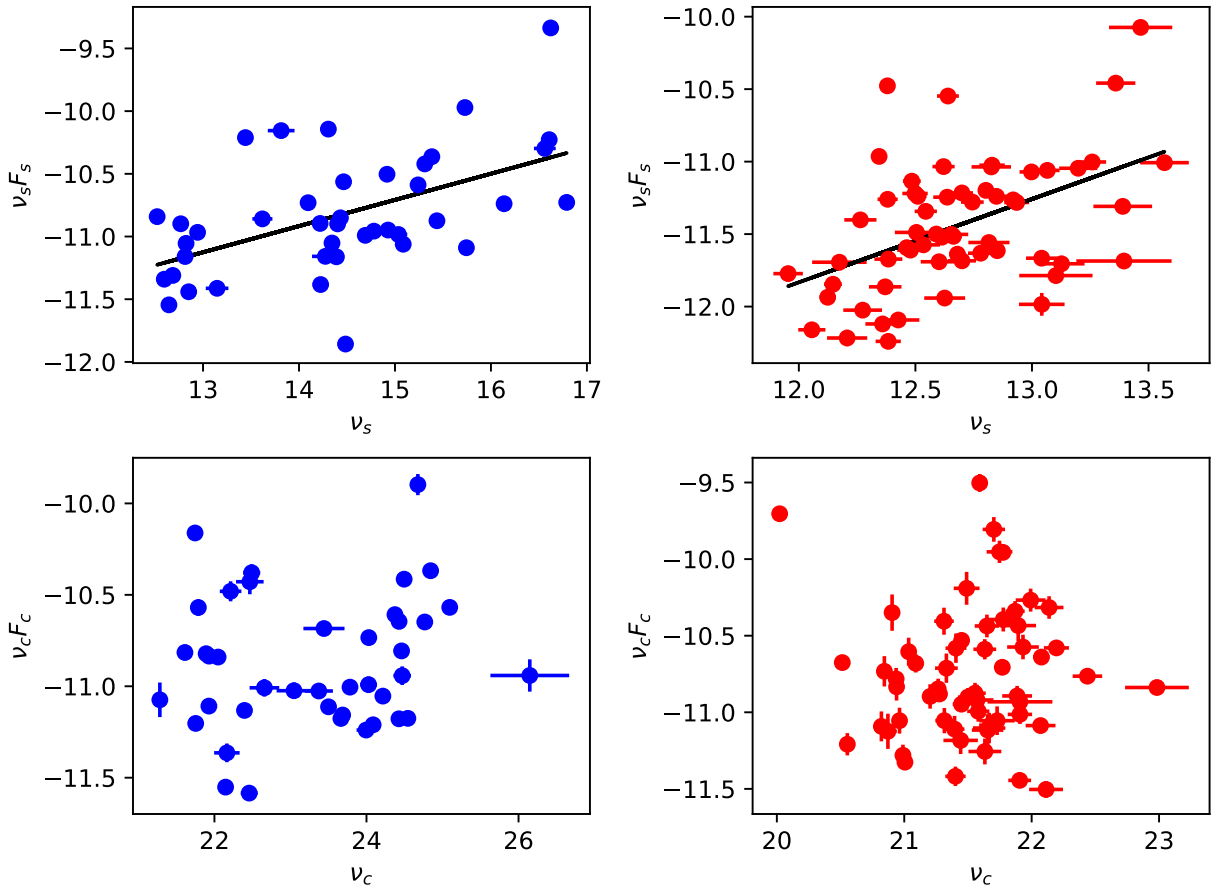


Figure 6. The relationship between spectral peak frequency and peak flux of polynomial. The *upper panels* show the relationship between synchrotron peak frequency ν_s and synchrotron peak flux $\nu_s F_s$, whereas the *lower panels* show IC peak frequency ν_s and IC peak flux $\nu_c F_c$. BL Lacs are shown by blue circles and FSRQs are shown by red circles. The solid lines represent the best linear regression fit.

changes in the SED (F. Massaro et al. 2008). Individual sources usually show a positive relationship

between peak frequency and luminosity and such a bluer-when-brighter trend of blazar may arise due to

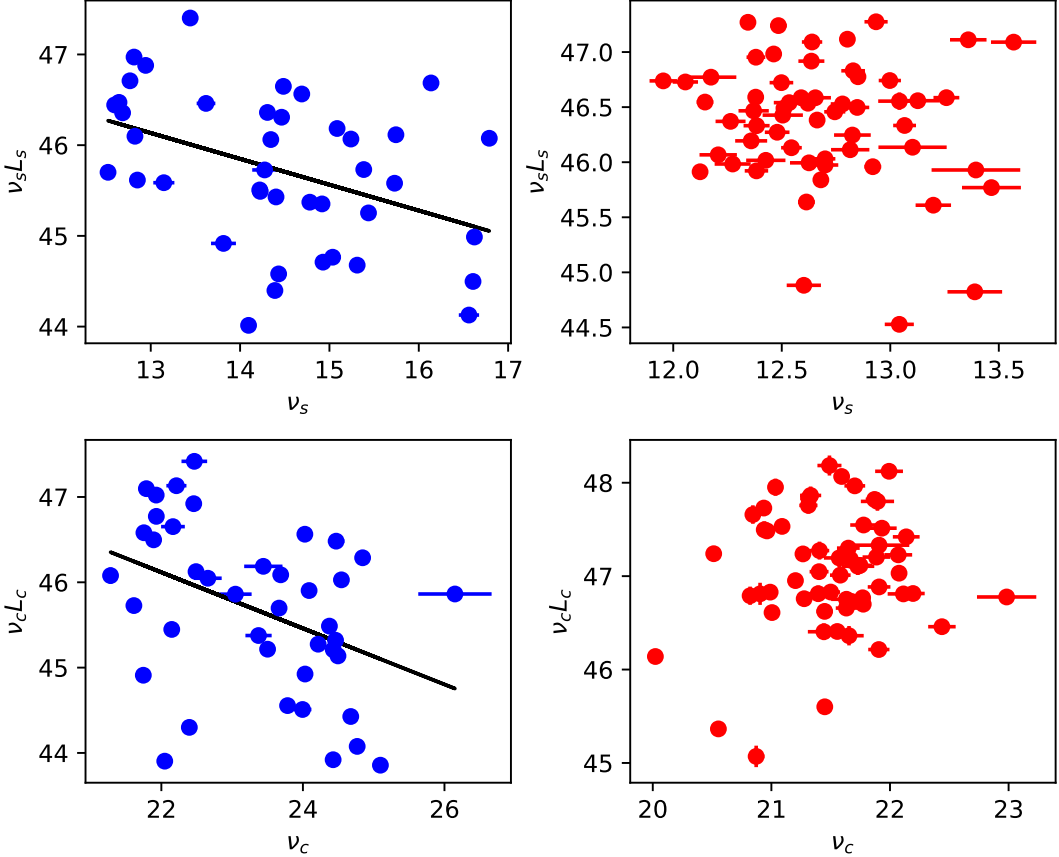


Figure 7. The relationship between spectral frequency and luminosity of polynomial. The *upper panels* show the relationship between synchrotron frequency ν_s and synchrotron luminosity L_s , whereas the *lower panels* show the relationship between IC peak frequency ν_c and IC peak luminosity L_c . BL Lacs are shown by blue circles and FSRQs are shown by red circles. The solid lines represent the best linear regression fit.

a single parameter, for example, the changing Doppler factor δ (Y. Feng et al. 2022). A negative trend in the $\nu_s - \nu_s L_s$ plane cannot be explained by independent jet parameters and suggests that some jet source parameters might be related to each other.

Figure 9 shows that the synchrotron frequency ν_s is tightly correlated with electron peak energy γ_{3p} with correlation coefficient $r_p \approx 0.9$ and chance probability $p \leq 10^{-18}$, however, it does not show any correlation with the parameter $B\delta$. The BL Lacs and FSRQs show the best linear relationship $\log \nu_s = 1.62 \log \gamma_{3p} + 7.80$ and $\log \nu_s = 1.56 \log \gamma_{3p} + 8.02$, respectively, closer to theoretical relation $\nu_s \sim \gamma_{3p}^2$. This confirms that synchrotron frequency shifts in the $\nu_s - \nu_s L_s$ plane are primarily caused by variations of particle energy γ_{3p} , whereas the parameter $B\delta$ is irrelevant. The synchrotron luminosity L_s inversely correlates with Doppler factor δ and source size R , as shown in Figure 10, showing that δ and R are inversely related.

Therefore, the luminosity in $\nu_s - \nu_s L_s$ plane should evolve mainly due to the internal relationship between the other jet parameters, namely, the magnetic field B , electron density n_e , and electron peak energy γ_{3p} . The relationship of γ_{3p} with n_e and B is shown in Figure 11. For BL Lacs, the particle energy γ_{3p} seems to be significantly inversely relationship with particle density n_e with coefficient $r_p < -0.8$, showing the best fit relationship $\log n_e = -1.35 \log \gamma_{3p} + 5.4$. The γ_{3p} also shows a negative correlation with B , with best fit relationship $\log B = -0.53 \log \gamma_{3p} + 0.6$. Similarly, the magnetic field B is positively correlated with density n_e through a linear relation $\log n_e = 1.32 \log B + 1.85$ with $r_p = -0.63$ and $p \simeq 10^{-6}$, and negatively correlated with δ , as shown in Figure 12. The FSRQs do not show these systematic trends, indicating that the jet parameters might be varying independently.

The relationship between parameters magnetic field B , electron energy γ_{3p} , and density n_e show, for BL

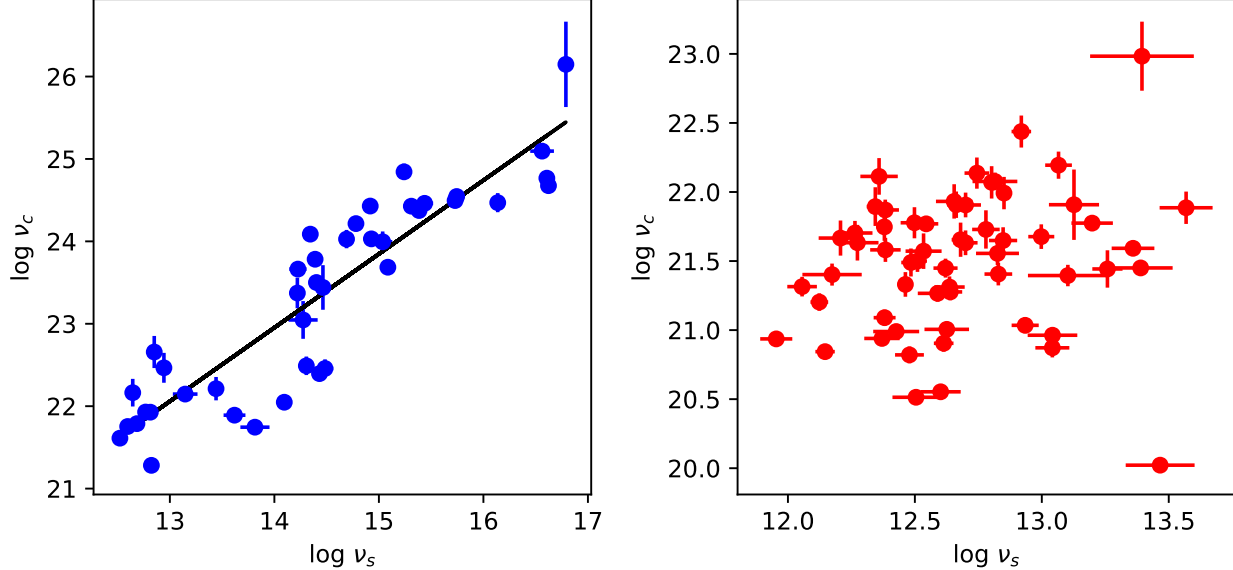


Figure 8. The relationship between synchrotron peak frequency ν_s and IC peak frequency ν_c . BL Lacs are shown by blue circles and FSRQs are shown by red circles. The solid lines represent the linear regression fit.

Lacs, that jet parameters in BL Lacs must be internally linked and explains the observed negative trend in $\nu_s - \nu_s L_s$ plan in context of equipartition (G. Ghisellini & F. Tavecchio 2008). In the equipartition scenario, the magnetic field energy density $U_B = B^2/8\pi$ and particle energy density $U_e \approx n_e \gamma_{3p} m_e c^2$ are correlated (i.e., $U_B \approx U_e$), leading to the constraint $B^2 \simeq n_e \gamma_{3p}$. Thus, the magnetic field B should be positively correlated with n_e and/or γ_{3p} , forcing an inverse relationship between γ_{3p} and n_e , to hold the equipartition. Consequently, an increasing frequency $\nu_s \propto \gamma_{3p}^2$ manifests a decrease in the luminosity $\nu_s L_s \propto n_e$. Figure 11 shows the negative relation between γ_{3p} and n_e and confirms this scenario for BL Lacs. The BL Lacs, on average, show a Compton Dominance ($C_D \sim 1$), which is another observational indicator that the physical conditions might be steady, dominated by equipartition. The FSRQs do not show such linear trends, indicating that the underlying physical conditions deviate significantly from the equipartition scenario. This difference might be related to the fact that the EC emission in FSRQs is sensitive to ambient environment, e.g. external photon fields, whereas the SSC emission in BL Lacs is unrelated to ambient environment.

4.2. Acceleration in Blazars

To investigate the statistical nature of particle acceleration in a combined acceleration+cooling scenario, we study how the synchrotron spectral curvature b_s evolves with synchrotron frequency ν_s . We find that ν_s significantly anti-correlates with b_s , for both the

BL Lacs and FSRQ, as shown in Figure 13, suggesting that stochastic nature of the underlying acceleration is general for all blazars. Such inverse correlation has been found in previous studies for large samples (see, e.g., L. Chen 2014; R. Xue et al. 2016). The best regression fit for BL Lacs yields $b_s = -0.03 \log \nu_s + 0.56$, whereas the FSRQs show $b_s = -0.07 \log \nu_s + 1.08$. The slope is usually different for different blazar classes (S. L. Luo et al. 2017), suggesting that physical conditions or nature of acceleration mechanism might be slightly different in FSRQs and BL Lacs. H. Xiao et al. (2024) showed that the blazars with low IC peak frequency follow the stochastic acceleration, whereas the high IC peak sources follow the energy-dependent acceleration mechanism, with the transition at $\nu_s \approx 10^{15}$. The IC peak frequency ν_c show a different behavior against its spectral curvature b_c . For BL Lacs, the ν_c and b_c show a positive relationship $b_c = 0.03 \log \nu_c - 0.62$ with $r_p = 0.66$ and $p \sim 10^{-6}$, whereas, the FSRQs show mildly negative relationship $b_c = -0.015 \log \nu_c + 0.41$ with $r_p = -0.38$ and $p \sim 10^{-3}$, as shown in Figure 13. This might be related to different nature of IC emission in two classes. The IC emission in FSRQs is more complicated than BL Lacs and arises as composite emission including both the SSC and EC components.

We investigate the evolution of source EED curvature r against its peak energy γ_{3p} , as shown in Figure 14. These EED parameters are intrinsic as compared to SED parameters b_s and ν_s and are not affected by other physical parameters, such as B or δ . Furthermore,

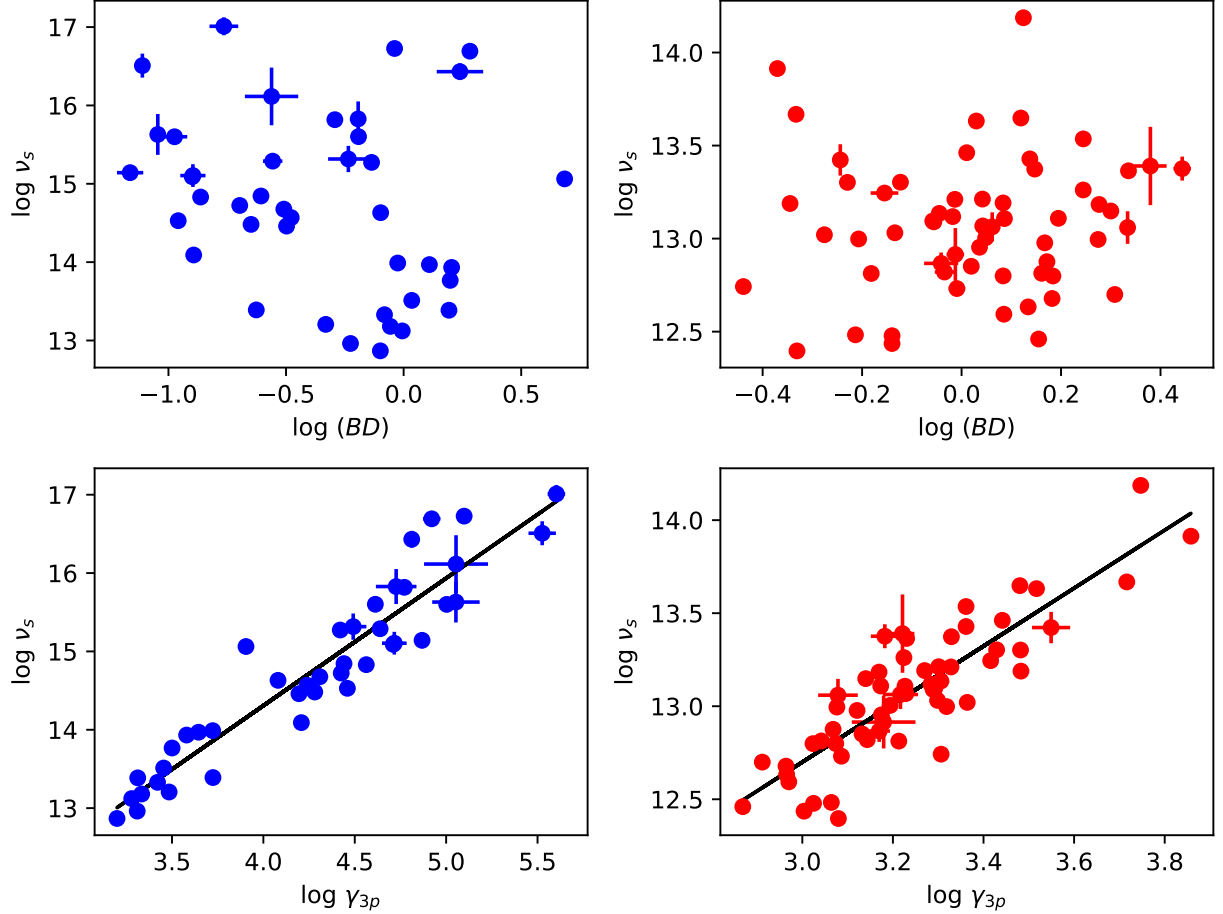


Figure 9. The relationship of synchrotron frequency ν_s with electron peak energy γ_{3p} (upper panels) and parameter $B\delta$ (lower panels), obtained by one-zone modeling. BL Lacs are shown by blue circles and FSRQs are shown by red circles. The solid lines represent the best linear regression fit.

the relationship between these intrinsic parameters reveals the relevance of specific processes and nature of magnetic turbulence during the evolution of EED. The $\gamma_{3p} - r$ plane shows the BL Lacs manifest a negative relationship $r = -0.075 \log \gamma_{3p} + 0.93$, whereas the FSRQs show a milder relationship with less significant correlation. This less significant correlation for FSRQs might be related to a relatively poor estimates of γ_{3p} and r due to several IC components involved, such as SSC and EC. High energy resolution data at X-rays might be necessary to resolve these components. Thus, the blazars show the intrinsic signature of stochastic acceleration, i.e., an inverse relationship between peak energy γ_{3p} and curvature r M. S. Anjum et al. (2020). However, a small slope < -0.1 and a large scatter, however, shows that the cooling must be relevant and the curvature might evolve in a nearly steady state conditions, where cooling tightly competes against acceleration and the negative trend in $\gamma_{3p} - r$ plane is affected (A. Tramacere et al. 2011). This is especially

true when the magnetic turbulence is softer than the hard-sphere ($q = 2$), such as, a Kolmogorov or Kraichnan turbulence with turbulence index $q < 2$. A. Tramacere et al. (2011) showed that a softer magnetic turbulence with index $q < 2$ is not an efficient accelerator as compared to the hard-sphere turbulence with $q = 2$, for which the acceleration is independent of particle energy and dominates the cooling.

We compare the SED curvature b_s with the EED curvature r by dividing our blazar sample into SSC and EC classes. In our work, the photon curvature b_s is constrained by polynomial fitting of synchrotron bump, whereas the sources EED curvature r is constrained by one-zone model fitting of entire SED. E. Massaro et al. (2006) found that an LP EED nearly yields an LP synchrotron SED and the ratio of photon and electron curvature parameters (b_s/r) varies from 0.18 to 0.22, depending on how b_s is measured. They recommend a nominal value $b_s/r = 0.2$, leading to the relationship

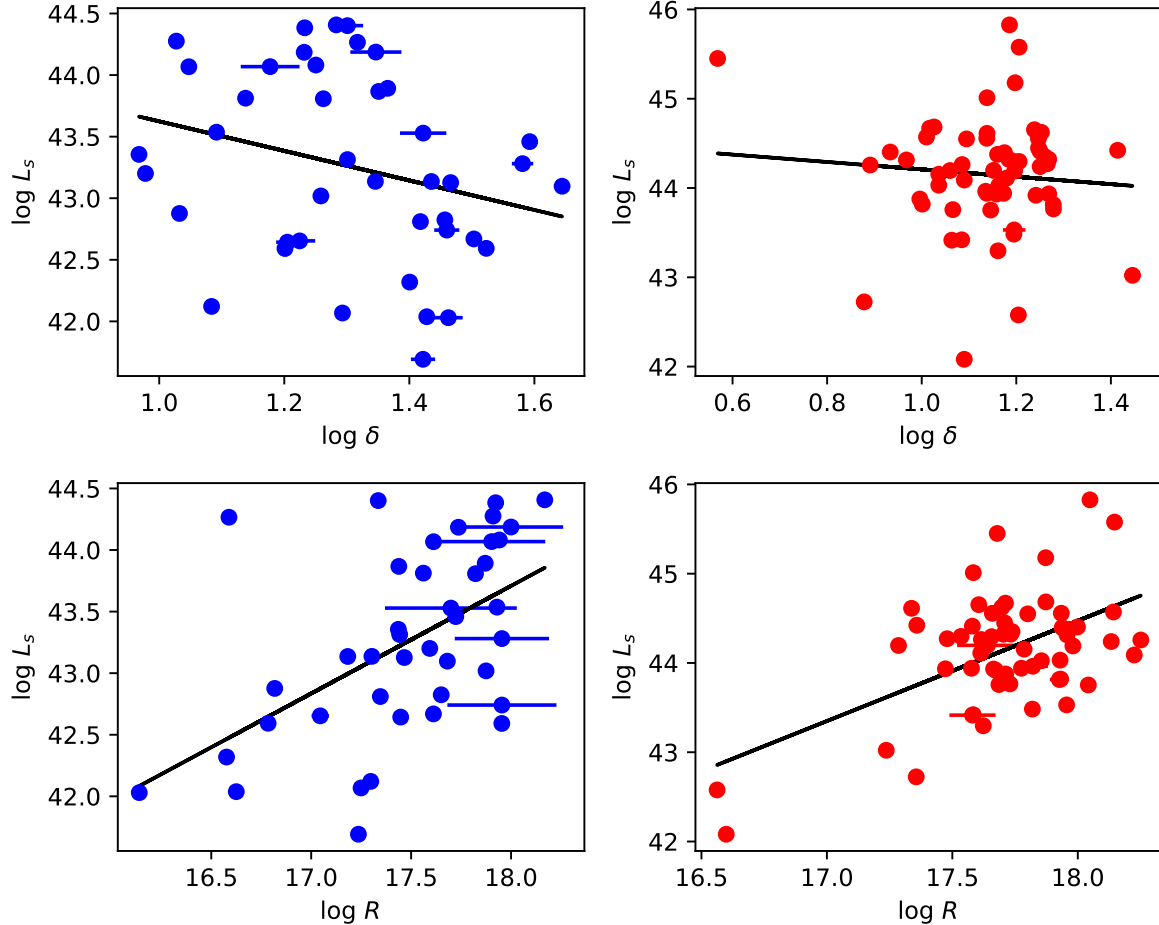


Figure 10. The relationship of synchrotron luminosity L_s with Doppler factor δ (upper panels), and source size R (lower panels), obtained by one-zone modeling. BL Lacs are shown by blue circles and FSRQs are shown by red circles. The solid lines represent the best linear regression fit.

$r = 5b_s$. We find that the SSC blazars (BL Lacs) show a best linear relationship $r \approx 4.2b_s$, closer to the expected relationship $r = 5b_s$, with correlation parameters $r_p > 0.5$ and $p \sim 10^{-3}$, as shown in Figure 15, indicating that the SED curvature in BL Lacs is a true indicator of source EED curvature r . The slight deviation from $r = 5b_s$ could be related to the fact the relationship $r = 5b_s$ was derived by polynomial fitting within a small frequency window around peak frequency ν_s , whereas we used broadband spectral data. On the other side, the EC blazars (FSRQs) show a mild relationship $r \approx 0.8b_s$ and a very weak correlation. The large deviation from $r = 5b_s$, for FSRQs, seem to arise due to a relatively poor estimation of b_s due to presence of thermal BBB in the synchrotron spectra. Moreover, when the spectral window of polynomial fitting is different than that of physical model fitting, the relationship between b_s and r is significantly deviates from $r = 5b_s$. Removing these

biases would require high quality multiband IR-to-UV spectral data.

5. DISCUSSION & SUMMARY

We systematically fit the nearly simultaneous broadband SEDs of an adequately large Fermi bright blazar sample with 4FGL-DR3 γ -ray data in the GeV-TeV band to study the spectral evolution of blazars. The blazars shows a negative trend in both the $\nu_s - \nu_s L_s$ and $\nu_s - b_s$ planes, however, these trends have been studied independently previously. We investigate the evolution of the synchrotron SED in both of these planes in a combined scenario including the nonthermal cooling and stochastic acceleration. We find that the blazar SEDs can be reproduced self-consistently by a leptonic one-zone model with LP EED. The GeV-TeV γ -ray emission of the ISP/HSP blazars is fitted satisfactorily by the SED model component, whereas, practically all LSP blazars essentially need an EC component based on external dusty torus to explain

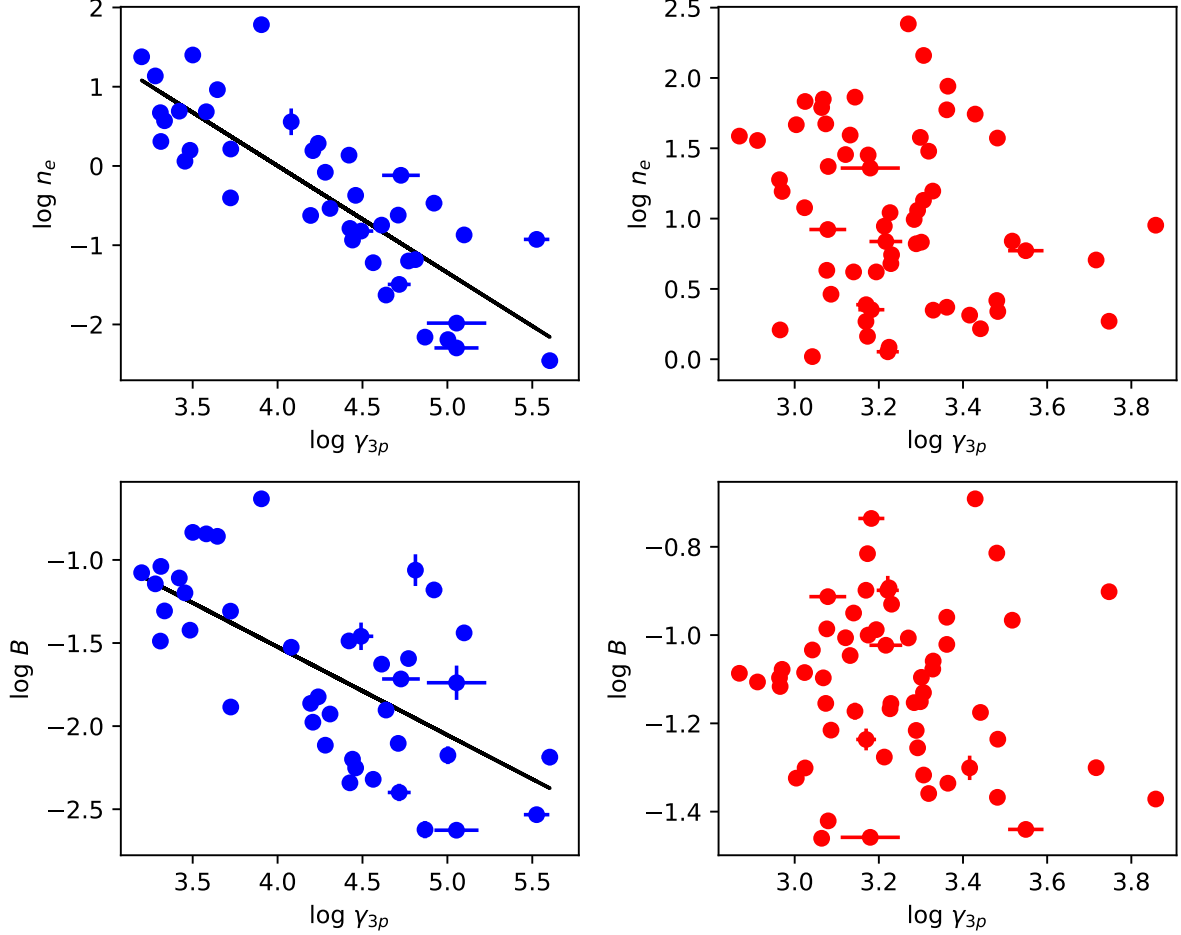


Figure 11. The relationship of particle energy γ_{3p} with particle density n_e (*upper panels*), and magnetic field B (*lower panels*). BL Lacs are shown by blue circles and FSRQs are shown by red circles. The solid lines represent the best linear regression fit.

the γ -ray emission. For a few LSP sources, a BLR component might be required to fit the high-energy tail of Fermi-LAT spectra, indicating that the energy dissipation location in blazars should be inside dusty torus photon field but closer to the edge of BLR. For some highly luminous Compton-dominated FSRQs, the dust torus component completely dominates the SSC, suggesting that the the SSC component might be irrelevant for such sources. Moreover, the location of the blob R_b from the central black hole is correlated with the disk luminosity, for FSRQs, indicating that the location of energy dissipation might be an indicator of accretion power and, thus, γ -ray power.

The electron energy γ_{3p} seems to be the dominant driver of synchrotron frequency ν_s , whereas magnetic field B and Doppler factor δ almost play no role, indicating that synchrotron frequency shifts in the blazar SED mainly arise due to the variation of particle energy γ_{3p} . The BL Lacs show a negative trend in the

$\nu_s - \nu_s L_s$ SED plane, known as blazar sequence. Such a spectral behavior of the BL Lacs in seems to be dominated by equipartition scenario, corresponding to stable jet configurations with minimum jet energy budget requirement and a maximum radiative efficiency. The internal relationship between the γ_{3p} , n_e , and B can explain the observed blazar sequence in the $\nu_s - \nu_s L_s$ plane (G. Ghisellini & F. Tavecchio 2008). We find that the BL Lacs seem to follow the equipartition $U_B \sim U_e$, forcing the constraint $\gamma_{3p} \propto 1/n_e$. Thus, when Doppler changes are irrelevant, the negative trend in $\nu_s - \nu_s L_s$ plane can naturally arise due to equipartition constraints, corresponding to the near steady state jet conditions. Thus, in a combined scenario, while an increase in particle energy γ_{3p} derives the synchrotron frequency, the luminosity gets lower due to a corresponding decrease in particle density n_e . The FSRQs do not show such equipartition constraints, indicating that jet parameters in these sources might be changing more independently, most likely due to

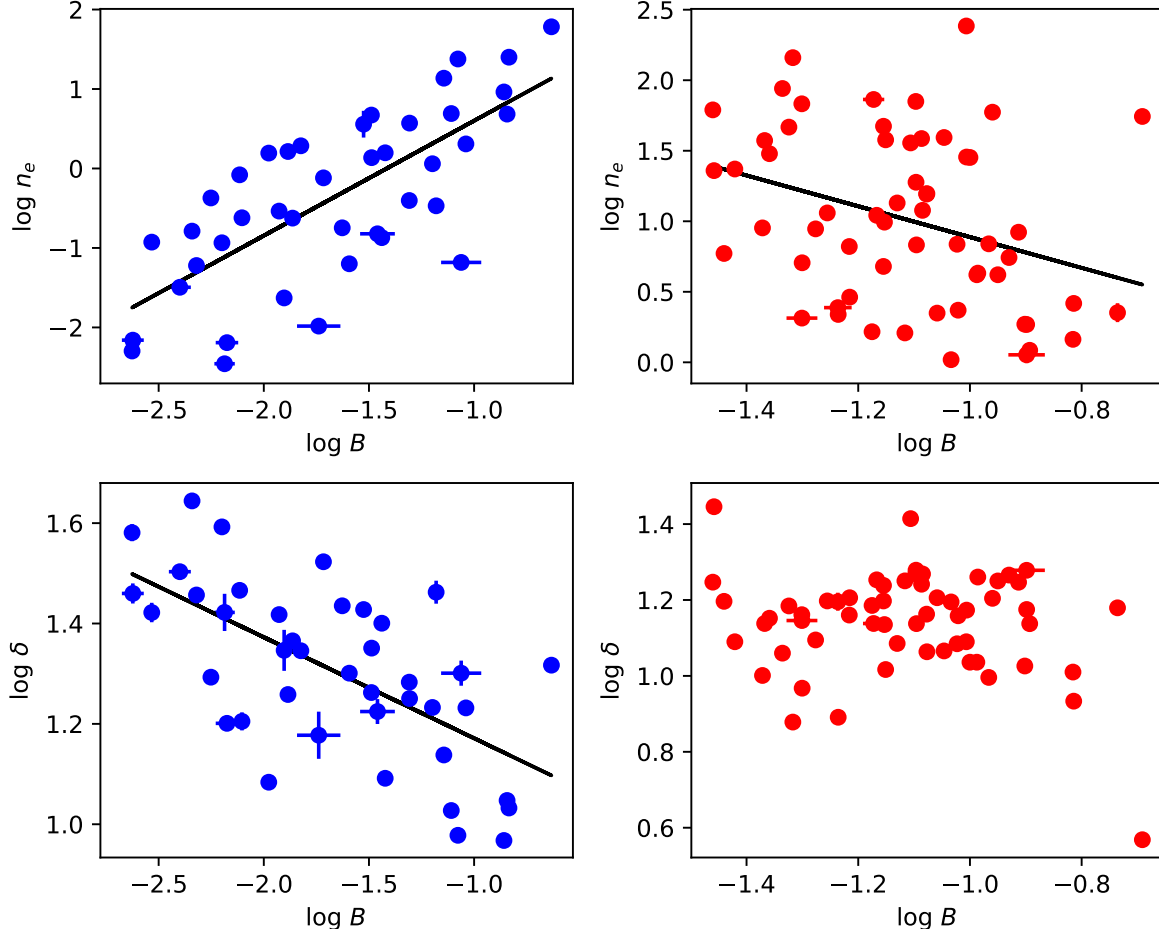


Figure 12. The relationship of magnetic field B with Doppler factor δ (*upper panels*) and particle density n_e (*lower panels*). BL Lacs are shown by blue circles and FSRQs are shown by red circles. The solid lines represent the best linear regression fit.

variable ambient conditions.

We find that the synchrotron frequency ν_s and the synchrotron spectral curvature b_s of blazars are negatively related, however, the slope is slightly different for BL Lacs and FSRQ. This confirms the stochastic nature of particle acceleration in the blazar jets. The hallmark of stochastic acceleration is the negative relationship between intrinsic EED parameters, namely, the electron peak energy γ_{3p} and electron curvature parameter r . The $\gamma_{3p} - r$ plane shows an indication of anti-correlation, thus, the negative trend observed in the $\nu_s - b_s$ plane seems to manifested in $\gamma_{3p} - r$ plane. However, the negative relationship is mild, especially for FSRQs. In the hard-sphere acceleration, the γ_{3p} and r are tightly inversely related. Thus, a deviation from strong hard-sphere acceleration suggests that the physical conditions in the blazar jet should be near to steady state, consistent with equipartition, and the magnetic turbulence might be soft, either Kraichnan or kolmogorov

type with turbulence index $q < 2$. The soft turbulence is not an efficient accelerator and the electron curvature r only mildly correlates with peak energy γ_{3p} (A. Tramacere et al. 2011). The synchrotron photon curvature b_s is generally an indicator of source electron curvature r and, within a small energy window, the two curvature parameters are found to be related as $r = 5b_s$. We find the relationship $r \approx 4b_s$ for BL Lacs, closer to the theoretical relationship $r = 5b_s$, as compared to FSRQs which show a mild relationship $r \approx b_s$. The significantly large deviation from $r = 5b_s$ for FSRQs might be related to the presence of thermal BBB in the synchrotron SED and slightly different energy windows in which b_s and r are measured. High energy resolution broadband spectra data of FSRQs might be required to tightly constrain the spectral curvature.

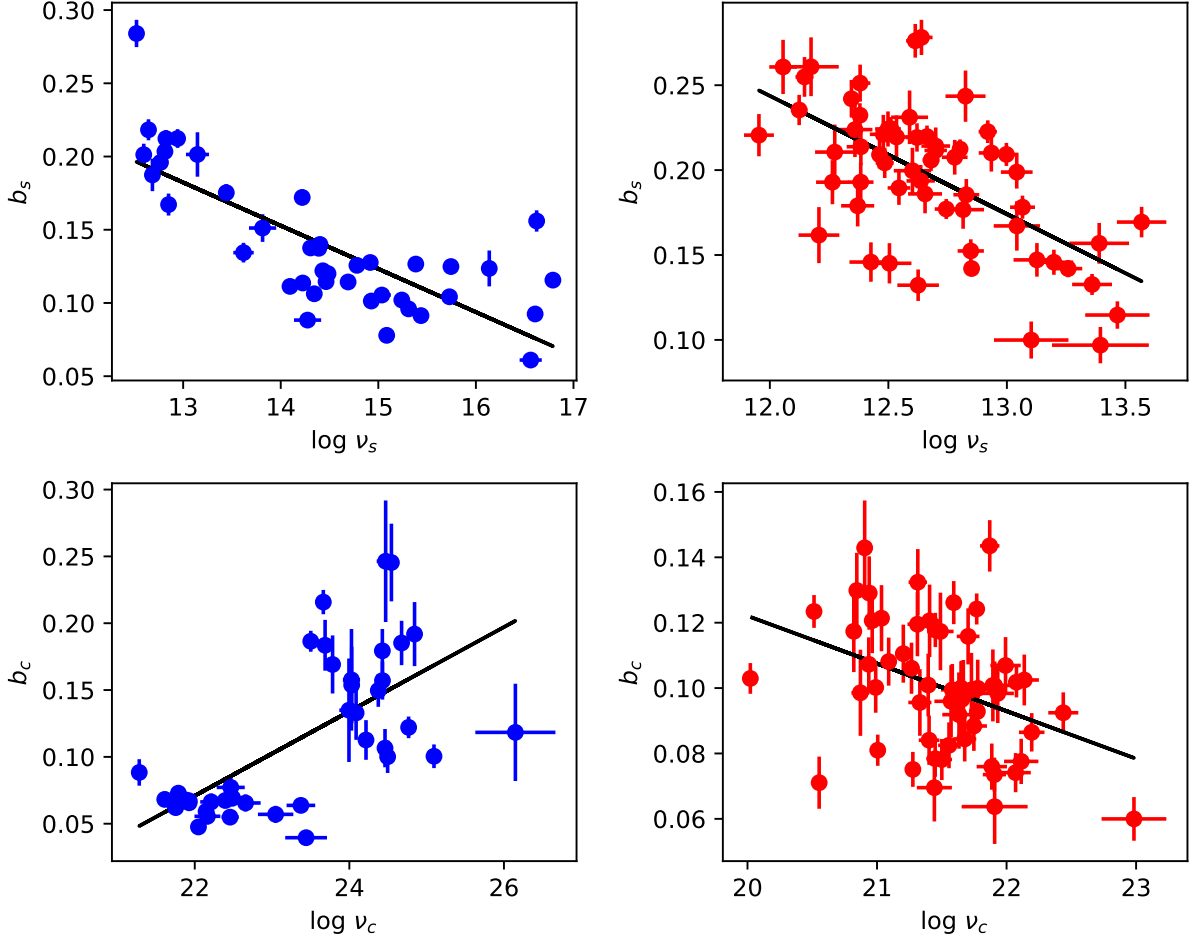


Figure 13. The relationship between the peak frequency and spectral curvature. The *upper panels* show the relationship between synchrotron frequency ν_s and synchrotron curvature b_s , whereas the *lower panels* show the relationship between IC frequency ν_c and IC curvature b_c . BL Lacs are shown by blue circles and FSRQs are shown by red circles. The solid lines represent the linear regression fit.

ACKNOWLEDGMENTS

We thank the editor and the anonymous referee for providing important insights and useful suggestions to improve this work. This work is supported by the Natural Science Foundation of Henan Province (242300420261), Key scientific research projects of colleges and universities in Henan Province (24a160001), and National Natural Science Foundation of China (grant No. U1938116). LC is supported by the National Science Foundation of China (grant 12173066). MFG is supported by the Na-

tional Science Foundation of China (grant 12473019). Both LC and MFG are supported by the National SKA Program of China (grant No. 2022SKA0120102), the Shanghai Pilot Program for Basic Research-Chinese Academy of Science, Shanghai Branch (JCYJ-SHFY-2021-013), and the China Manned Space Project with No. CMS-CSST-2025-A07.

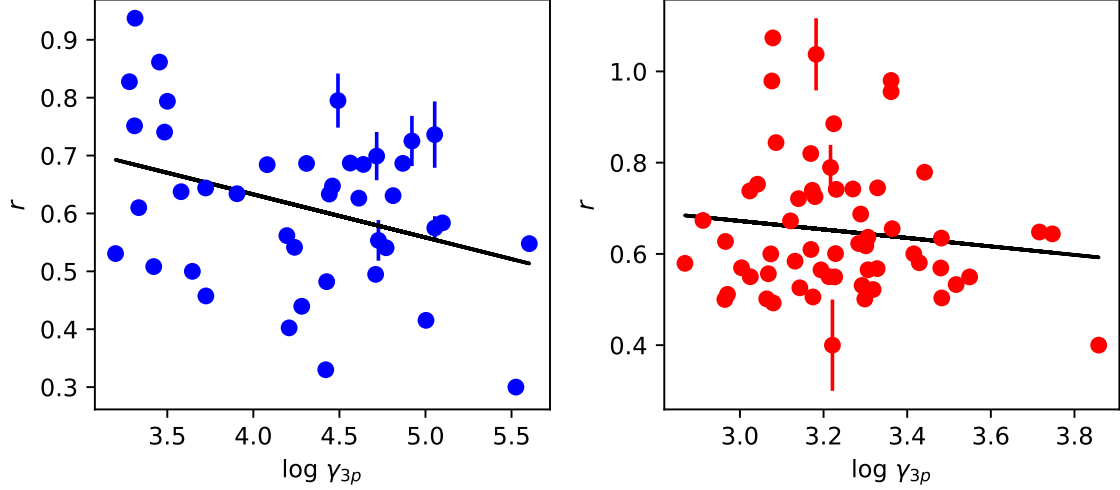


Figure 14. The intrinsic signature of stochastic acceleration, i.e., the relationship between EED peak energy γ_{3p} and its curvature r . BL Lacs are shown by blue circles and FSRQs are shown by red circles. The solid lines represent the linear regression fit.

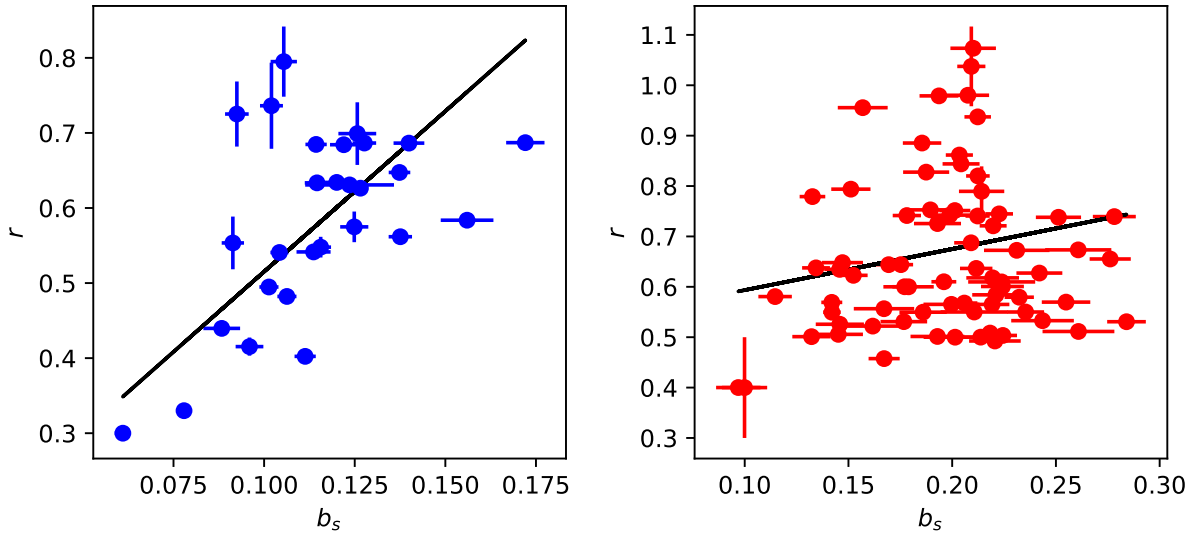


Figure 15. The relationship between synchrotron spectral curvature b_s and source electron curvature r . The SSC blazars are shown by blue circles and the EC blazars are shown by red circles. The solid lines represent the linear regression fit.

Table 1. Parameters of Log-parabolic Polynomial Fitting for BL Lacs.

Name	Association	SED	z	b_s	ν_s	$\nu_s F_s$	$\nu_s L_s$	b_c	ν_c	$\nu_c F_c$	$\nu_c L_c$	C_D
(1)	(2)	(3)	(4)	(5)	(6)	(7)	(8)	(9)	(10)	(11)	(12)	(13)
0033.5-1921	KUV00311-1938	HSP	0.61	0.12	15.74	-11.09	46.11	0.25	24.54	-11.18	46.03	0.82
0050.7-0929	PKS0048-09	HSP	0.634	0.08	15.09	-11.06	46.18	0.18	23.69	-11.16	46.09	0.8
0120.4-2701	1Jy0118-272	ISP	0.56	0.11	14.34	-11.05	46.06	0.13	24.09	-11.21	45.9	0.69
0136.5+3906	B30133+388	HSP	0.75	0.12	16.14	-10.74	46.69	0.25	24.47	-10.94	46.48	0.63

Table 1 *continued*

Table 1 (*continued*)

Name	Association	SED	z	b_s	ν_s	$\nu_s F_s$	$\nu_s L_s$	b_c	ν_c	$\nu_c F_c$	$\nu_c L_c$	C_D
(1)	(2)	(3)	(4)	(5)	(6)	(7)	(8)	(9)	(10)	(11)	(12)	(13)
0222.6+4302	3C66A	ISP	0.444	0.11	14.46	-10.56	46.31	0.04	23.44	-10.68	46.19	0.76
0238.6+1637	PKS0235+164	LSP	0.94	0.19	12.69	-11.31	46.36	0.07	21.79	-10.57	47.1	5.51
0303.4-2407	PKS0301-243	ISP	0.26	0.13	14.78	-10.96	45.37	0.11	24.22	-11.05	45.27	0.8
0334.2-4008	PKS0332-403	LSP	1.445	0.2	12.81	-11.16	46.97	0.07	21.93	-11.11	47.02	1.12
0428.6-3756	PKS0426-380	LSP	1.11	0.21	12.94	-10.97	46.88	0.08	22.47	-10.43	47.42	3.45
0449.4-4350	PKS0447-439	HSP	0.205	0.13	15.38	-10.36	45.73	0.15	24.37	-10.61	45.49	0.57
0507.9+6737	1ES0502+675	HSP	0.416	0.12	16.79	-10.73	46.08	0.12	26.15	-10.94	45.86	0.61
0516.7-6207	PKS0516-621	LSP	1.3	0.22	12.64	-11.54	46.47	0.06	22.16	-11.36	46.65	1.52
0538.8-4405	PKS0537-441	LSP	0.894	0.18	13.44	-10.21	47.4	0.07	22.21	-10.48	47.13	0.54
0700.5-6610	PKS0700-661	ISP	0.26	0.14	14.4	-10.9	45.43	0.19	23.5	-11.11	45.22	0.61
0712.7+5033	GB6J0712+5033	LSP	0.502	0.2	13.15	-11.41	45.59	0.06	22.15	-11.55	45.45	0.73
0721.9+7120	S50716+714	ISP	0.31	0.14	14.31	-10.14	46.36	0.07	22.49	-10.38	46.13	0.58
0738.1+1742	PKS0735+17	ISP	0.45	0.09	14.27	-11.16	45.73	0.06	23.05	-11.02	45.86	1.36
0818.2+4222	S40814+425	LSP	0.53	0.17	12.85	-11.44	45.62	0.07	22.66	-11.01	46.05	2.7
1015.0+4926	1H1013+498	HSP	0.212	0.09	15.44	-10.87	45.25	0.11	24.46	-10.81	45.32	1.17
1054.5+2211	SDSSJ105430.62+2	ISP	2.05	0.12	14.48	-11.86	46.65	0.05	22.46	-11.58	46.92	1.88
1058.4+0133	4C01.28	LSP	0.89	0.2	12.77	-10.9	46.71	0.07	21.93	-10.84	46.77	1.16
1058.6+5627	RXJ10586+5628	HSP	0.143	0.11	15.04	-10.98	44.76	0.13	24.0	-11.24	44.51	0.56
1058.6-8003	PKS1057-79	LSP	0.581	0.21	12.82	-11.05	46.1	0.09	21.28	-11.07	46.08	0.96
1104.4+3812	MKN421	HSP	0.03	0.16	16.62	-9.34	44.99	0.19	24.68	-9.9	44.43	0.28
1147.0-3812	PKS1144-379	LSP	1.048	0.2	12.6	-11.34	46.44	0.06	21.75	-11.2	46.58	1.37
1217.9+3007	ON325	HSP	0.13	0.1	14.93	-10.95	44.71	0.15	24.03	-10.73	44.92	1.64
1221.5+2814	ON231	ISP	0.102	0.12	14.43	-10.85	44.58	0.07	22.4	-11.13	44.3	0.52
1248.3+5820	PG1246+586	ISP	0.847	0.11	14.69	-10.99	46.56	0.16	24.03	-10.99	46.56	1.0
1253.2+5301	S41250+53	ISP	0.445	0.11	14.23	-11.38	45.49	0.22	23.66	-11.18	45.7	1.61
1427.0+2348	PG1424+240	HSP	0.16	0.13	14.92	-10.5	45.35	0.16	24.43	-10.65	45.21	0.72
1517.7-2422	APLIB	ISP	0.048	0.11	14.09	-10.73	44.01	0.05	22.05	-10.84	43.9	0.78
1543.0+6130	1RXSJ154256.6+6	ISP	0.117	0.14	14.39	-11.16	44.4	0.17	23.78	-11.0	44.55	1.44
1555.7+1111	PG1553+113	HSP	0.36	0.1	15.24	-10.59	46.07	0.19	24.84	-10.37	46.29	1.66
1653.8+3945	MKN501	HSP	0.034	0.06	16.56	-10.3	44.13	0.1	25.09	-10.57	43.86	0.54
1751.5+0938	OT081	LSP	0.322	0.28	12.52	-10.84	45.7	0.07	21.61	-10.82	45.73	1.06
1800.6+7828	S51803+784	LSP	0.68	0.13	13.62	-10.86	46.46	0.07	21.89	-10.82	46.5	1.09
2000.0+6508	1ES1959+650	HSP	0.047	0.09	16.61	-10.23	44.5	0.12	24.77	-10.65	44.08	0.38
2009.4-4849	1Jy2005-489	HSP	0.071	0.1	15.31	-10.42	44.68	0.18	24.43	-11.18	43.92	0.18
2139.4-4235	MH2136-428	ISP	0.28	0.17	14.22	-10.9	45.51	0.06	23.37	-11.03	45.38	0.74
2158.8-3013	PKS2155-304	HSP	0.116	0.1	15.73	-9.97	45.58	0.1	24.5	-10.41	45.14	0.36
2202.7+4216	BLLAC	ISP	0.069	0.15	13.81	-10.16	44.92	0.06	21.75	-10.16	44.91	0.99

NOTE— Column (1) gives the source name (4FGL J). Column (2) gives the source association. Column (3) gives the SED type of source based on spectral fitting. Column (4) gives the redshift of the source. Column (5-8) gives the curvature, peak frequency, peak flux, and peak luminosity of the synchrotron bump, respectively. Column (9-12) gives the curvature, peak frequency, peak flux, and peak luminosity of the IC bump, respectively. Column (13) shows Compton dominance (ratio of IC to synchrotron peak flux).

Table 2. Parameters of Log-parabolic Polynomial Fitting for FSRQs.

Name	Association	SED	z	b_s	ν_s	$\nu_s F_s$	$\nu_s L_s$	b_c	ν_c	$\nu_c F_c$	$\nu_c L_c$	C_D
(1)	(2)	(3)	(4)	(5)	(6)	(7)	(8)	(9)	(10)	(11)	(12)	(13)
0017.5-0514	PMNJ0017-0512	LSP	0.227	0.2	13.04	-11.67	44.53	0.1	20.87	-11.12	45.07	3.48
0051.1-0648	PKS0048-071	LSP	1.975	0.26	12.17	-11.69	46.77	0.08	21.4	-11.42	47.05	1.89
0118.9-2141	PKS0116-219	LSP	1.165	0.22	12.66	-11.52	46.38	0.1	21.91	-11.01	46.88	3.18
0137.0+4751	OC457	LSP	0.859	0.22	12.62	-11.03	46.54	0.08	21.45	-10.95	46.62	1.22
0145.0-2732	PKS0142-278	LSP	1.148	0.22	12.48	-11.61	46.27	0.12	20.82	-11.09	46.79	3.3
0205.0-1700	PKS0202-17	LSP	1.74	0.18	12.37	-11.86	46.47	0.13	20.94	-10.83	47.5	10.72
0210.7-5101	PKS0208-512	LSP	1.003	0.15	12.85	-11.24	46.5	0.1	21.65	-10.44	47.3	6.35
0217.8+0144	PKS0215+015	LSP	1.715	0.21	12.8	-11.2	47.12	0.07	22.07	-11.09	47.23	1.29
0221.1+3556	B20218+357	LSP	0.944	0.18	12.82	-11.56	46.11	0.1	22.08	-10.64	47.03	8.29
0229.5-3644	PKS0227-369	LSP	2.115	0.17	13.04	-11.98	46.55	0.12	20.96	-11.05	47.48	8.51
0237.8+2848	4C28.07	LSP	1.213	0.22	12.5	-11.22	46.72	0.1	21.78	-10.39	47.55	6.69
0245.9-4650	PKS0244-470	LSP	1.385	0.23	12.59	-11.5	46.59	0.11	21.27	-10.85	47.24	4.49
0349.8-2103	PKS0347-211	LSP	2.944	0.26	12.06	-12.16	46.73	0.13	21.31	-11.05	47.83	12.76
0407.0-3826	PKS0405-385	LSP	1.285	0.21	12.38	-11.67	46.33	0.1	21.58	-10.99	47.01	4.78
0423.3-0120	PKS0420-01	LSP	0.916	0.28	12.64	-10.55	47.09	0.08	21.28	-10.88	46.76	0.46
0457.0-2324	PKS0454-234	LSP	1.003	0.18	12.74	-11.28	46.46	0.1	22.14	-10.32	47.42	9.19
0530.9+1332	PKS0528+134	LSP	2.06	0.22	11.95	-11.77	46.74	0.11	20.94	-10.78	47.73	9.79
0654.4+4514	S40650+45	LSP	0.933	0.21	12.7	-11.68	45.97	0.07	21.91	-11.44	46.21	1.74
0730.3-1141	PKS0727-11	LSP	1.591	0.24	12.34	-10.96	47.27	0.1	21.89	-10.43	47.8	3.39
0824.7+5552	OJ535	LSP	1.417	0.15	12.43	-12.09	46.02	0.1	20.99	-11.28	46.83	6.48
0920.9+4441	S40917+44	LSP	2.19	0.21	12.46	-11.59	46.98	0.1	21.33	-10.71	47.86	7.61
0948.9+0022	PMNJ0948+0022	LSP	0.585	0.28	12.61	-11.52	45.64	0.14	20.9	-10.35	46.81	14.86
0957.6+5523	4C55.17	LSP	0.896	0.1	13.39	-11.69	45.93	0.06	22.98	-10.84	46.78	7.04
1012.7+2439	B21011+25	LSP	1.634	0.15	13.13	-11.7	46.56	0.06	21.91	-10.93	47.33	5.93
1016.0+0512	TXS1013+054	LSP	1.713	0.22	12.36	-12.12	46.19	0.08	22.11	-11.5	46.81	4.13
1033.9+6050	S41030+61	LSP	1.401	0.17	13.57	-11.01	47.09	0.08	21.89	-10.89	47.2	1.3
1129.8-1447	PKS1127-145	LSP	1.184	0.15	12.5	-11.49	46.43	0.12	20.51	-10.68	47.24	6.5
1159.5+2914	4C29.45	LSP	0.729	0.18	13.07	-11.06	46.33	0.09	22.19	-10.58	46.81	3.02
1229.0+0202	3C273	LSP	0.158	0.11	13.47	-10.07	45.77	0.1	20.02	-9.7	46.14	2.35
1246.7-2548	PKS1244-255	LSP	0.635	0.21	12.7	-11.22	46.03	0.1	21.63	-10.59	46.66	4.24
1256.1-0547	3C279	LSP	0.536	0.23	12.38	-10.48	46.59	0.09	21.75	-9.95	47.12	3.35
1310.5+3221	1Jy1308+326	LSP	0.997	0.22	12.51	-11.24	46.49	0.08	21.5	-10.9	46.83	2.18
1332.0-0509	PKS1329-049	LSP	2.15	0.21	12.93	-11.28	47.27	0.12	21.03	-10.6	47.95	4.76
1354.8-1041	PKS1352-104	LSP	0.332	0.2	12.6	-11.69	44.88	0.07	20.55	-11.21	45.36	3.03
1457.4-3539	PKS1454-354	LSP	1.424	0.22	12.53	-11.57	46.54	0.1	21.57	-10.92	47.2	4.51
1504.4+1029	PKS1502+106	LSP	1.84	0.14	12.85	-11.61	46.78	0.11	21.99	-10.27	48.12	22.21
1510.8-0542	PKS1508-05	LSP	1.191	0.1	13.1	-11.79	46.14	0.1	21.4	-11.11	46.81	4.75
1512.8-0906	PKS1510-08	LSP	0.36	0.15	13.2	-11.05	45.61	0.09	21.77	-9.96	46.7	12.3
1522.1+3144	B21520+31	LSP	1.487	0.19	12.38	-12.24	45.92	0.14	21.87	-10.34	47.82	79.39
1553.6+1257	PKS1551+130	LSP	1.29	0.21	12.27	-12.02	45.98	0.09	21.63	-11.26	46.75	5.87
1625.7-2527	PKS1622-253	LSP	0.786	0.19	12.54	-11.34	46.13	0.12	21.77	-10.71	46.77	4.33
1635.2+3808	4C38.41	LSP	1.814	0.2	12.48	-11.13	47.24	0.12	21.49	-10.19	48.18	8.79
1640.4+3945	NRAO512	LSP	1.666	0.16	12.21	-12.22	46.07	0.1	21.67	-11.1	47.18	13.0
1848.4+3217	B21846+32A	LSP	0.789	0.21	12.68	-11.64	45.84	0.1	21.65	-11.12	46.36	3.33
1849.2+6705	4C66.20	LSP	0.657	0.24	12.83	-11.04	46.25	0.08	21.56	-10.88	46.41	1.45

Table 2 *continued*

Table 2 (*continued*)

Name	Association	SED	z	b_s	ν_s	$\nu_s F_s$	$\nu_s L_s$	b_c	ν_c	$\nu_c F_c$	$\nu_c L_c$	C_D
(1)	(2)	(3)	(4)	(5)	(6)	(7)	(8)	(9)	(10)	(11)	(12)	(13)
1911.2-2006	1908-201	LSP	1.119	0.19	12.83	-11.02	46.83	0.12	21.41	-10.58	47.27	2.78
1923.5-2104	PMNJ1923-2104	LSP	0.874	0.14	13.26	-11.0	46.59	0.07	21.44	-11.18	46.4	0.66
2025.6-0735	PKS2023-07	LSP	1.388	0.19	12.65	-11.5	46.59	0.1	21.93	-10.57	47.51	8.48
2056.2-4714	PKS2052-47	LSP	1.489	0.19	12.64	-11.25	46.92	0.12	21.31	-10.41	47.76	6.92
2143.5+1743	S32141+17	LSP	0.213	0.16	13.39	-11.31	44.82	0.12	21.45	-10.53	45.6	6.0
2147.1+0931	1Jy2144+092	LSP	1.113	0.24	12.12	-11.94	45.91	0.11	21.2	-10.9	46.95	10.94
2157.5+3127	B22155+31	LSP	1.486	0.21	12.78	-11.63	46.53	0.1	21.73	-11.05	47.11	3.78
2203.4+1725	PKS2201+171	LSP	1.076	0.21	13.0	-11.07	46.74	0.08	21.68	-11.08	46.73	0.97
2207.5-5346	PKS2204-54	LSP	1.206	0.13	12.63	-11.94	45.99	0.08	21.01	-11.33	46.61	4.13
2229.7-0832	PKS2227-08	LSP	1.56	0.25	12.38	-11.26	46.95	0.11	21.09	-10.68	47.53	3.8
2232.6+1143	CTA102	LSP	1.037	0.19	12.26	-11.4	46.37	0.12	21.7	-9.81	47.97	39.43
2253.9+1609	3C454.3	LSP	0.859	0.13	13.36	-10.46	47.11	0.13	21.59	-9.5	48.07	9.03
2327.5+0939	PKS2325+093	LSP	1.843	0.25	12.15	-11.85	46.55	0.13	20.84	-10.73	47.66	12.99
2345.2-1555	PMNJ2345-1555	LSP	0.621	0.22	12.92	-11.26	45.96	0.09	22.44	-10.76	46.46	3.16

NOTE— Column (1-13) are same as in 1.

Table 3. One-zone IC Model Jet Parameters of BL Lacs.

Name	SED	z	R_{17}	B	δ	n_e	$\gamma_{\min,2}$	γ_0	$\gamma_{\max,6}$	s	r
(1)	(2)	(3)	(4)	(5)	(6)	(7)	(8)	(9)	(10)	(11)	(12)
0033.5-1921	HSP	0.61	8.0	0.018	15.04	0.01	4.5	19977.0	1.3	2.13	0.57
0050.7-0929	HSP	0.634	2.74	0.033	22.44	1.37	1.7	6002.0	9.4	2.58	0.33
0120.4-2701	ISP	0.56	4.8	0.005	44.09	0.16	3.5	427.0	1.1	1.27	0.48
0136.5+3906	HSP	0.75	2.17	0.087	20.0	0.07	1.0	17108.0	4.6	2.27	0.63
0222.6+4302	ISP	0.444	5.29	0.006	39.13	0.12	2.0	5126.0	2.4	2.07	0.63
0238.6+1637	LSP	0.94	3.64	0.072	13.74	13.68	0.4	370.0	0.0	1.82	0.83
0303.4-2407	ISP	0.26	4.09	0.004	31.86	0.03	5.0	8252.0	4.4	1.88	0.7
0334.2-4008	LSP	1.445	8.38	0.063	17.09	1.15	0.4	448.0	0.0	1.62	0.86
0428.6-3756	LSP	1.11	5.45	0.091	17.05	2.04	0.1	1493.0	0.0	2.74	0.94
0449.4-4350	HSP	0.205	1.52	0.024	27.24	0.18	1.6	20851.0	1.6	2.63	0.63
0507.9+6737	HSP	0.416	5.0	0.007	26.43	0.0	3.6	14347.0	3.9	1.42	0.55
0516.7-6207	LSP	1.3	8.12	0.078	10.65	4.91	0.4	1142.0	0.0	2.63	0.51
0538.8-4405	LSP	0.894	14.75	0.049	19.19	0.4	0.2	905.0	0.0	2.01	0.64
0700.5-6610	ISP	0.26	2.22	0.012	26.17	0.29	2.8	58.0	1.0	-0.5	0.69
0712.7+5033	LSP	0.502	2.73	0.139	9.28	9.18	0.1	1181.0	0.0	2.43	0.5
0721.9+7120	ISP	0.31	7.43	0.014	23.2	0.24	2.0	266.0	5.7	1.01	0.56
0738.1+1742	ISP	0.45	2.92	0.008	29.25	0.83	5.0	1468.0	0.4	2.02	0.44
0818.2+4222	LSP	0.53	7.5	0.013	18.14	1.64	0.5	971.0	0.0	2.33	0.46
1015.0+4926	HSP	0.212	0.61	0.019	33.35	0.76	1.8	16606.0	0.6	2.44	0.55
1054.5+2211	ISP	2.05	0.39	0.233	20.75	60.63	0.5	140.0	0.8	0.77	0.63
1058.4+0133	LSP	0.89	8.74	0.049	17.8	3.72	0.0	600.0	0.0	2.32	0.61
1058.6+5627	HSP	0.143	1.11	0.035	16.77	0.15	3.0	10880.0	1.9	2.28	0.8
1058.6-8003	LSP	0.581	8.5	0.038	12.35	1.58	0.3	1166.0	0.0	2.38	0.74

Table 3 *continued*

Table 3 (*continued*)

Name	SED	z	R_{17}	B	δ	n_e	$\gamma_{\min,2}$	γ_0	$\gamma_{\max,6}$	s	r
(1)	(2)	(3)	(4)	(5)	(6)	(7)	(8)	(9)	(10)	(11)	(12)
1104.4+3812	HSP	0.03	0.38	0.036	25.15	0.13	1.4	15494.0	2.4	1.94	0.58
1147.0-3812	LSP	1.048	6.64	0.032	18.3	4.7	0.1	864.0	0.0	2.44	0.75
1217.9+3007	HSP	0.13	2.8	0.008	16.03	0.24	4.2	315.0	6.7	0.81	0.49
1221.5+2814	ISP	0.102	0.42	0.03	26.78	3.61	0.8	183.0	3.7	0.51	0.68
1248.3+5820	ISP	0.847	10.0	0.012	22.21	0.02	3.6	1782.0	2.2	1.1	0.68
1253.2+5301	ISP	0.445	2.01	0.015	22.17	1.93	1.6	800.0	9.3	1.55	0.54
1427.0+2348	HSP	0.16	9.0	0.002	28.83	0.01	4.1	1580.0	2.9	0.71	0.69
1517.7-2422	ISP	0.048	1.99	0.011	12.13	1.56	3.2	501.0	4.3	1.79	0.4
1543.0+6130	ISP	0.117	1.78	0.006	19.64	0.43	4.8	614.0	6.9	0.84	0.65
1555.7+1111	HSP	0.36	9.0	0.002	38.11	0.01	4.2	34583.0	2.1	2.24	0.74
1653.8+3945	HSP	0.034	1.72	0.003	26.42	0.12	2.2	17928.0	19.4	2.24	0.3
1751.5+0938	LSP	0.322	3.92	0.084	9.51	23.86	0.2	722.0	0.0	2.64	0.53
1800.6+7828	LSP	0.68	4.09	0.143	11.15	4.83	0.2	646.0	0.0	2.02	0.64
2000.0+6508	HSP	0.047	0.14	0.066	29.0	0.34	1.4	15211.0	2.8	1.93	0.73
2009.4-4849	HSP	0.071	8.99	0.007	15.89	0.01	3.1	25260.0	1.2	2.5	0.42
2139.4-4235	ISP	0.28	4.47	0.005	28.63	0.06	5.3	1797.0	0.3	1.2	0.69
2158.8-3013	HSP	0.116	2.77	0.026	20.0	0.06	1.0	21131.0	1.3	2.52	0.54
2202.7+4216	ISP	0.069	0.66	0.146	10.77	25.13	0.3	1384.0	0.0	2.43	0.79

NOTE— Column (1) gives the source name (4FGL J). Column (2) gives the SED type of source. Column (2) gives the redshift of the source. Column (4) gives the source size in 10^{17} cm. Column (8) gives the minimum energy of EED in 10^2 . Column (9) gives the reference energy of EED peak energy. Column (10) gives the maximum energy of EED in 10^6 .

Table 4. One-zone IC Model Jet Parameters of FSRQs.

Name	z	R_{17}	B	n_e	Γ	δ	γ_{\min}	$\gamma_{0,2}$	$\gamma_{\max,4}$	s	r	$R_{b,18}$	$R_{T,19}$	$L_{D,45}$
(1)	(2)	(3)	(4)	(5)	(6)	(7)	(8)	(9)	(10)	(11)	(12)	(13)	(14)	(15)
0017.5-0514	0.227	0.4	0.1	242.4	7.0	12.3	2.8	8.1	5.0	2.46	0.74	0.4	0.4	0.33
0051.1-0648	1.975	7.2	0.08	15.6	8.84	14.5	24.9	3.8	9.0	2.6	0.51	6.8	3.3	27.97
0118.9-2141	1.165	3.8	0.11	4.2	28.0	17.8	25.2	7.8	5.0	2.65	0.72	4.5	1.8	7.69
0137.0+4751	0.859	8.5	0.1	4.2	6.0	10.9	39.0	5.2	7.0	2.46	0.57	8.4	1.7	7.04
0145.0-2732	1.148	4.8	0.09	39.3	6.52	11.6	2.2	5.0	2.0	2.49	0.58	4.6	2.8	19.32
0205.0-1700	1.74	4.0	0.07	47.2	30.0	17.3	3.3	3.5	3.0	2.36	0.6	3.8	6.5	106.02
0210.7-5101	1.003	6.6	0.07	9.9	8.06	13.7	3.5	7.0	6.0	2.45	0.62	6.3	3.1	23.87
0217.8+0144	1.715	8.7	0.13	1.9	9.24	15.0	13.5	6.8	4.0	2.45	0.82	8.9	14.8	545.24
0221.1+3556	0.944	4.5	0.06	11.5	27.79	15.8	12.4	5.5	8.0	2.42	0.53	4.3	6.2	96.07
0229.5-3644	2.115	3.0	0.08	70.7	15.0	18.6	9.4	3.5	6.0	2.42	0.56	3.9	3.2	26.14
0237.8+2848	1.213	7.4	0.07	4.8	36.26	15.8	30.1	5.4	6.0	2.4	0.6	7.6	2.3	13.46
0245.9-4650	1.385	3.8	0.1	28.5	9.19	14.9	10.6	4.5	10.0	2.38	0.67	3.6	3.9	37.77
0349.8-2103	2.944	2.3	0.08	35.9	45.0	26.0	33.2	4.2	5.0	2.61	0.67	2.3	5.1	63.88
0407.0-3826	1.285	5.4	0.08	18.9	17.11	19.0	2.6	2.9	6.0	2.5	0.5	5.1	1.8	8.5
0423.3-0120	0.916	13.9	0.15	1.5	5.59	10.2	22.8	7.5	4.0	2.56	0.74	13.3	2.4	15.0
0457.0-2324	1.003	11.0	0.05	2.1	7.31	14.0	2.3	3.3	3.0	1.92	0.6	13.4	1.3	4.5

Table 4 *continued*

Table 4 (*continued*)

Name	z	R_{17}	B	n_e	Γ	δ	γ_{\min}	$\gamma_{0,2}$	$\gamma_{\max,4}$	s	r	$R_{b,18}$	$R_{T,19}$	$L_{D,45}$
(1)	(2)	(3)	(4)	(5)	(6)	(7)	(8)	(9)	(10)	(11)	(12)	(13)	(14)	(15)
0530.9+1332	2.06	16.8	0.04	23.5	7.0	12.3	2.5	2.7	7.0	2.37	0.49	16.0	5.2	67.24
0654.4+4514	0.933	3.8	0.09	6.9	6.89	12.2	4.6	4.3	5.0	2.07	0.79	3.8	1.2	3.62
0730.3-1141	1.591	13.6	0.08	1.6	10.0	17.8	47.3	3.5	7.0	2.46	0.63	16.4	10.1	253.4
0824.7+5552	1.417	3.8	0.07	73.0	45.0	13.7	2.4	1.3	10.0	1.9	0.53	4.4	2.8	19.4
0920.9+4441	2.19	9.2	0.06	6.6	8.77	14.5	14.8	4.7	5.0	2.15	0.69	8.9	5.0	62.98
0948.9+0022	0.585	1.9	0.05	87.4	24.15	11.5	20.5	6.0	3.0	2.23	0.66	1.8	1.4	5.0
0957.6+5523	0.896	8.5	0.04	9.0	5.99	10.0	2.1	11.9	10.0	2.37	0.4	8.2	1.9	8.7
1012.7+2439	1.634	9.1	0.05	5.1	5.0	9.3	22.1	7.5	5.0	1.91	0.65	8.9	7.5	140.09
1016.0+0512	1.713	9.0	0.06	2.4	10.0	15.7	3.5	1.6	10.0	1.81	0.61	8.8	2.8	20.0
1033.9+6050	1.401	7.5	0.13	1.9	5.84	10.6	47.8	7.4	10.0	1.87	0.64	7.3	5.8	85.19
1129.8-1447	1.184	6.1	0.1	28.3	6.0	10.9	24.4	1.1	4.0	1.85	0.51	5.8	4.5	51.32
1159.5+2914	0.729	3.0	0.12	5.5	25.0	18.4	4.1	6.4	6.0	2.37	0.74	3.3	0.3	0.27
1229.0+0202	0.158	4.8	0.2	55.3	7.78	3.7	19.7	4.0	3.0	2.04	0.58	4.8	3.4	28.86
1246.7-2548	0.635	4.1	0.07	13.5	16.59	12.2	9.1	8.0	3.0	2.49	0.64	4.0	2.0	9.79
1256.1-0547	0.536	4.7	0.08	38.6	13.38	17.4	11.1	2.7	2.0	2.49	0.58	4.5	0.4	0.5
1310.5+3221	0.997	17.8	0.06	2.2	4.13	7.8	47.7	6.2	10.0	2.3	0.5	17.0	2.8	20.03
1332.0-0509	2.15	4.6	0.12	8.4	12.77	17.7	15.6	4.3	6.0	2.04	1.07	4.1	5.0	61.67
1354.8-1041	0.332	2.3	0.05	144.6	4.0	7.6	8.4	6.1	10.0	2.41	0.57	2.3	1.1	2.78
1457.4-3539	1.424	6.0	0.08	6.8	8.13	13.7	21.8	5.8	5.0	2.34	0.62	5.9	5.2	68.87
1504.4+1029	1.84	9.6	0.04	5.9	10.04	15.7	9.5	5.3	5.0	2.1	0.55	13.2	1.3	4.05
1510.8-0542	1.191	8.4	0.13	1.1	17.0	19.0	6.5	3.9	42.0	2.5	0.4	9.6	4.5	49.73
1512.8-0906	0.36	2.2	0.04	37.4	45.0	13.7	11.1	3.6	10.0	1.82	0.63	2.6	1.1	2.82
1522.1+3144	1.487	1.7	0.03	22.9	23.85	27.9	23.8	2.3	6.0	1.81	0.73	1.7	1.3	4.26
1553.6+1257	1.29	6.3	0.05	8.8	23.7	12.4	33.5	3.6	7.0	2.28	0.55	7.5	4.0	39.46
1625.7-2527	0.786	6.6	0.09	1.0	9.98	15.7	50.0	2.1	4.0	1.93	0.75	6.3	0.6	1.0
1635.2+3808	1.814	14.0	0.06	2.9	35.0	16.1	4.5	5.1	4.0	2.36	0.84	13.3	4.4	48.54
1640.4+3945	1.666	4.4	0.04	30.1	19.49	14.2	15.0	4.9	8.0	2.35	0.52	4.3	3.2	25.3
1848.4+3217	0.789	3.8	0.08	15.7	6.92	11.6	5.5	6.0	3.0	2.37	0.57	4.0	1.0	2.31
1849.2+6705	0.657	5.2	0.11	6.9	5.38	9.9	24.2	5.2	10.0	2.14	0.53	7.4	2.0	10.34
1911.2-2006	1.119	8.6	0.13	1.2	11.0	13.7	25.7	6.1	1.0	2.22	0.89	10.2	3.4	29.11
1923.5-2104	0.874	10.0	0.15	2.6	4.58	8.6	12.6	6.4	4.0	2.23	0.57	9.6	3.7	33.38
2025.6-0735	1.388	5.0	0.07	11.0	27.47	17.9	24.3	4.7	7.0	2.39	0.55	4.7	1.9	9.42
2056.2-4714	1.489	5.5	0.1	4.3	14.0	18.2	18.4	5.9	2.0	2.4	0.98	7.8	2.4	13.89
2143.5+1743	0.213	0.4	0.11	59.4	14.13	16.0	28.7	5.0	8.0	1.73	0.96	0.4	1.2	3.62
2147.1+0931	1.113	4.2	0.05	68.0	8.8	14.5	4.1	3.1	9.0	2.41	0.55	4.1	2.5	15.02
2157.5+3127	1.486	4.6	0.1	2.3	8.71	14.4	18.2	6.3	1.0	1.9	0.98	4.4	0.4	0.49
2203.4+1725	1.076	4.1	0.18	2.2	9.4	15.1	8.9	8.5	10.0	2.47	1.04	3.9	0.4	0.38
2207.5-5346	1.206	5.1	0.07	37.8	16.71	10.4	11.6	1.6	9.0	1.91	0.5	5.0	3.2	25.28
2229.7-0832	1.56	5.4	0.08	12.0	15.0	18.6	24.4	4.0	6.0	2.38	0.74	5.3	3.5	31.42
2232.6+1143	1.037	5.1	0.03	61.6	28.56	17.7	19.1	2.6	4.0	2.35	0.5	5.1	3.9	38.89
2253.9+1609	0.859	11.2	0.07	1.6	38.0	15.3	14.6	2.1	8.0	1.24	0.78	13.0	4.1	41.67
2327.5+0939	1.843	5.1	0.05	46.5	17.48	15.3	31.6	2.3	9.0	2.27	0.57	4.8	3.1	24.31
2345.2-1555	0.621	3.4	0.09	2.2	35.0	16.1	17.9	5.0	2.0	2.06	0.74	3.6	1.5	5.75

NOTE— Column (3) gives the source size R in 10^{17} cm. Column (8) gives the minimum energy of EED γ_{\min} in 10^2 . Column (10) gives the maximum energy γ_{\max} of EED in 10^4 . Column (13) gives the blob location R_b in 10^{18} cm. Column (14) gives the DT radius R_T in 10^{19} cm. Column (15) gives the disk luminosity in 10^{45} erg s $^{-1}$.

REFERENCES

- Abdo, A. A., Ackermann, M., Ajello, M., et al. 2009, ApJ, 700, 597, doi: [10.1088/0004-637X/700/1/597](https://doi.org/10.1088/0004-637X/700/1/597)
- Abdo, A. A., Ackermann, M., Agudo, I., et al. 2010, ApJ, 716, 30, doi: [10.1088/0004-637X/716/1/30](https://doi.org/10.1088/0004-637X/716/1/30)
- Abdollahi, S., Acero, F., Ackermann, M., et al. 2020, ApJS, 247, 33, doi: [10.3847/1538-4365/ab6bcb](https://doi.org/10.3847/1538-4365/ab6bcb)
- Ajello, M., Baldini, L., Ballet, J., et al. 2022, ApJS, 263, 24, doi: [10.3847/1538-4365/ac9523](https://doi.org/10.3847/1538-4365/ac9523)
- Anjum, M. S., Chen, L., & Gu, M. 2020, ApJ, 898, 48, doi: [10.3847/1538-4357/ab99a1](https://doi.org/10.3847/1538-4357/ab99a1)
- Blandford, R. D., & Rees, M. J. 1978, in BL Lac Objects, ed. A. M. Wolfe, 328–341
- Błażejowski, M., Sikora, M., Moderski, R., & Madejski, G. M. 2000, ApJ, 545, 107, doi: [10.1086/317791](https://doi.org/10.1086/317791)
- Bloom, S. D., & Marscher, A. P. 1996, ApJ, 461, 657, doi: [10.1086/177092](https://doi.org/10.1086/177092)
- Cerruti, M. 2020, Galaxies, 8, 72, doi: [10.3390/galaxies8040072](https://doi.org/10.3390/galaxies8040072)
- Chen, L. 2014, ApJ, 788, 179, doi: [10.1088/0004-637X/788/2/179](https://doi.org/10.1088/0004-637X/788/2/179)
- Chen, L. 2018, ApJS, 235, 39, doi: [10.3847/1538-4365/aab8fb](https://doi.org/10.3847/1538-4365/aab8fb)
- Costamante, L., Cutini, S., Tosti, G., Antolini, E., & Tramacere, A. 2018, MNRAS, 477, 4749, doi: [10.1093/mnras/sty887](https://doi.org/10.1093/mnras/sty887)
- D'Elia, V., Perri, M., Puccetti, S., et al. 2013, A&A, 551, A142, doi: [10.1051/0004-6361/201220863](https://doi.org/10.1051/0004-6361/201220863)
- Dermer, C. D., & Schlickeiser, R. 1993, ApJ, 416, 458, doi: [10.1086/173251](https://doi.org/10.1086/173251)
- Fan, J. H., Yang, J. H., Liu, Y., et al. 2016, ApJS, 226, 20, doi: [10.3847/0067-0049/226/2/20](https://doi.org/10.3847/0067-0049/226/2/20)
- Fan, J. H., Yang, J. H., Xiao, H. B., et al. 2017, ApJL, 835, L38, doi: [10.3847/2041-8213/835/2/L38](https://doi.org/10.3847/2041-8213/835/2/L38)
- Feng, Y., Hu, S., Zhou, R., & Gao, S. 2022, Universe, 8, 585, doi: [10.3390/universe8110585](https://doi.org/10.3390/universe8110585)
- Fossati, G., Maraschi, L., Celotti, A., Comastri, A., & Ghisellini, G. 1998, MNRAS, 299, 433, doi: [10.1046/j.1365-8711.1998.01828.x](https://doi.org/10.1046/j.1365-8711.1998.01828.x)
- Ghisellini, G., Celotti, A., Fossati, G., Maraschi, L., & Comastri, A. 1998, MNRAS, 301, 451, doi: [10.1046/j.1365-8711.1998.02032.x](https://doi.org/10.1046/j.1365-8711.1998.02032.x)
- Ghisellini, G., Maraschi, L., & Dondi, L. 1996, A&AS, 120, 503
- Ghisellini, G., & Tavecchio, F. 2008, MNRAS, 387, 1669, doi: [10.1111/j.1365-2966.2008.13360.x](https://doi.org/10.1111/j.1365-2966.2008.13360.x)
- Ghisellini, G., & Tavecchio, F. 2009, MNRAS, 397, 985, doi: [10.1111/j.1365-2966.2009.15007.x](https://doi.org/10.1111/j.1365-2966.2009.15007.x)
- Ghisellini, G., Tavecchio, F., Foschini, L., & Ghirlanda, G. 2011, MNRAS, 414, 2674, doi: [10.1111/j.1365-2966.2011.18578.x](https://doi.org/10.1111/j.1365-2966.2011.18578.x)
- Ghisellini, G., Tavecchio, F., Foschini, L., et al. 2010, MNRAS, 402, 497, doi: [10.1111/j.1365-2966.2009.15898.x](https://doi.org/10.1111/j.1365-2966.2009.15898.x)
- Giommi, P., Capalbi, M., Fiocchi, M., et al. 2002, in Blazar Astrophysics with BeppoSAX and Other Observatories, ed. P. Giommi, E. Massaro, & G. Palumbo, 63, doi: [10.48550/arXiv.astro-ph/0209596](https://doi.org/10.48550/arXiv.astro-ph/0209596)
- Giommi, P., Padovani, P., Polenta, G., et al. 2012, MNRAS, 420, 2899, doi: [10.1111/j.1365-2966.2011.20044.x](https://doi.org/10.1111/j.1365-2966.2011.20044.x)
- Hu, H.-B., Wang, H.-Q., Xue, R., Peng, F.-K., & Wang, Z.-R. 2024, MNRAS, 528, 7587, doi: [10.1093/mnras/stae522](https://doi.org/10.1093/mnras/stae522)
- Kang, S.-J., Chen, L., & Wu, Q. 2014, ApJS, 215, 5, doi: [10.1088/0067-0049/215/1/5](https://doi.org/10.1088/0067-0049/215/1/5)
- Kardashev, N. S. 1962, Soviet Ast., 6, 317
- Katarzyński, K., Ghisellini, G., Mastichiadis, A., Tavecchio, F., & Maraschi, L. 2006, A&A, 453, 47, doi: [10.1051/0004-6361:20054176](https://doi.org/10.1051/0004-6361:20054176)
- Konigl, A. 1981, ApJ, 243, 700, doi: [10.1086/158638](https://doi.org/10.1086/158638)
- Luo, S. L., Ding, N., Luo, D., Wang, X. P., & Zhang, X. 2017, Acta Astronomica Sinica, 58, 57
- Mannheim, K. 1993, A&A, 269, 67, doi: [10.48550/arXiv.astro-ph/9302006](https://doi.org/10.48550/arXiv.astro-ph/9302006)
- Maraschi, L., Ghisellini, G., & Celotti, A. 1992, ApJL, 397, L5, doi: [10.1086/186531](https://doi.org/10.1086/186531)
- Massaro, E., Perri, M., Giommi, P., & Nesci, R. 2004, A&A, 413, 489, doi: [10.1051/0004-6361:20031558](https://doi.org/10.1051/0004-6361:20031558)
- Massaro, E., Tramacere, A., Perri, M., Giommi, P., & Tosti, G. 2006, A&A, 448, 861, doi: [10.1051/0004-6361:20053644](https://doi.org/10.1051/0004-6361:20053644)
- Massaro, F., Tramacere, A., Cavaliere, A., Perri, M., & Giommi, P. 2008, A&A, 478, 395, doi: [10.1051/0004-6361:20078639](https://doi.org/10.1051/0004-6361:20078639)
- Mastichiadis, A., & Kirk, J. G. 1997, A&A, 320, 19, doi: [10.48550/arXiv.astro-ph/9610058](https://doi.org/10.48550/arXiv.astro-ph/9610058)
- Merloni, A., Lamer, G., Liu, T., et al. 2024, A&A, 682, A34, doi: [10.1051/0004-6361/202347165](https://doi.org/10.1051/0004-6361/202347165)
- Mücke, A., Protheroe, R. J., Engel, R., Rachen, J. P., & Stanev, T. 2003, Astroparticle Physics, 18, 593, doi: [10.1016/S0927-6505\(02\)00185-8](https://doi.org/10.1016/S0927-6505(02)00185-8)
- Nieppola, E., Tornikoski, M., & Valtaoja, E. 2006, A&A, 445, 441, doi: [10.1051/0004-6361:20053316](https://doi.org/10.1051/0004-6361:20053316)

- Nieppola, E., Valtaoja, E., Tornikoski, M., Hovatta, T., & Kotiranta, M. 2008, A&A, 488, 867,
doi: [10.1051/0004-6361:200809716](https://doi.org/10.1051/0004-6361:200809716)
- Planck Collaboration, Aatroskoski, J., Ade, P. A. R., et al. 2011, A&A, 536, A15, doi: [10.1051/0004-6361/201116466](https://doi.org/10.1051/0004-6361/201116466)
- Sikora, M. 1997, in American Institute of Physics Conference Series, Vol. 410, Proceedings of the Fourth Compton Symposium, ed. C. D. Dermer, M. S. Strickman, & J. D. Kurfess (AIP), 494–505,
doi: [10.1063/1.54010](https://doi.org/10.1063/1.54010)
- Sikora, M., Begelman, M. C., & Rees, M. J. 1994, ApJ, 421, 153, doi: [10.1086/173633](https://doi.org/10.1086/173633)
- Stratta, G., Capalbi, M., Giommi, P., et al. 2011, arXiv e-prints, arXiv:1103.0749, doi: [10.48550/arXiv.1103.0749](https://doi.org/10.48550/arXiv.1103.0749)
- Tan, C., Xue, R., Du, L.-M., et al. 2020, ApJS, 248, 27,
doi: [10.3847/1538-4365/ab8cc6](https://doi.org/10.3847/1538-4365/ab8cc6)
- Tavecchio, F., Maraschi, L., & Ghisellini, G. 1998, ApJ, 509, 608, doi: [10.1086/306526](https://doi.org/10.1086/306526)
- Tramacere, A. 2020,, Astrophysics Source Code Library, record ascl:2009.001
- Tramacere, A., Giommi, P., Perri, M., Verrecchia, F., & Tosti, G. 2009, A&A, 501, 879,
doi: [10.1051/0004-6361/200810865](https://doi.org/10.1051/0004-6361/200810865)
- Tramacere, A., Massaro, E., & Taylor, A. M. 2011, ApJ, 739, 66, doi: [10.1088/0004-637X/739/2/66](https://doi.org/10.1088/0004-637X/739/2/66)
- Tramacere, A., Massaro, F., & Cavalieri, A. 2007, A&A, 466, 521, doi: [10.1051/0004-6361:20066723](https://doi.org/10.1051/0004-6361:20066723)
- Urry, C. M., & Padovani, P. 1995, PASP, 107, 803,
doi: [10.1086/133630](https://doi.org/10.1086/133630)
- Xiao, H., Yang, W., Zhang, Y., et al. 2024, ApJ, 966, 99,
doi: [10.3847/1538-4357/ad38bd](https://doi.org/10.3847/1538-4357/ad38bd)
- Xue, R., Luo, D., Du, L. M., et al. 2016, MNRAS, 463, 3038, doi: [10.1093/mnras/stw2038](https://doi.org/10.1093/mnras/stw2038)
- Yan, D., Zeng, H., & Zhang, L. 2012, PASJ, 64, 80,
doi: [10.1093/pasj/64.4.80](https://doi.org/10.1093/pasj/64.4.80)
- Yang, J. H., Fan, J. H., Liu, Y., et al. 2022, ApJS, 262, 18,
doi: [10.3847/1538-4365/ac7deb](https://doi.org/10.3847/1538-4365/ac7deb)
- Zhou, R. X., Zheng, Y. G., Zhu, K. R., & Kang, S. J. 2021, ApJ, 915, 59, doi: [10.3847/1538-4357/abfe69](https://doi.org/10.3847/1538-4357/abfe69)

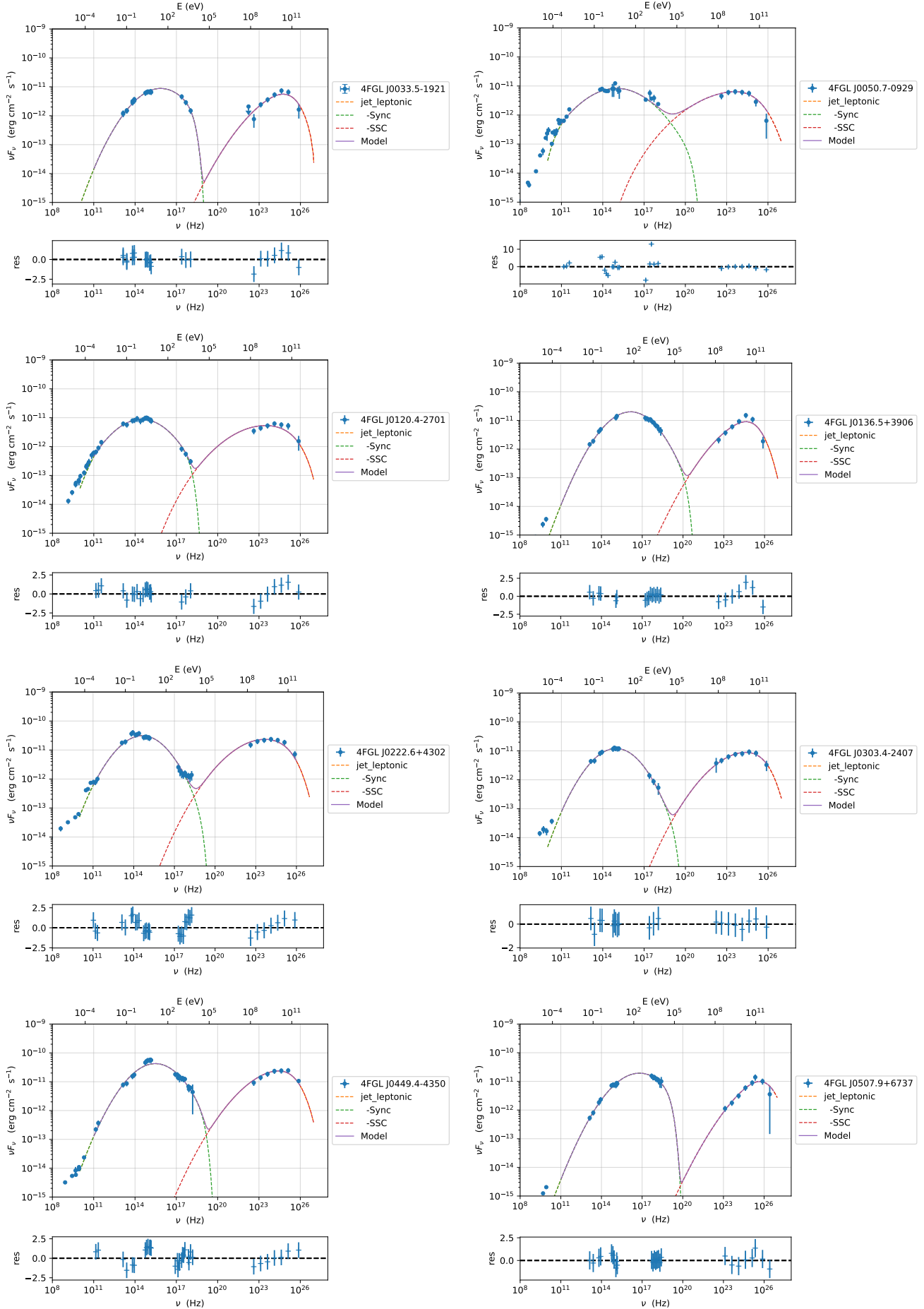


Figure 16. SED Modeling of SSC Blazars.

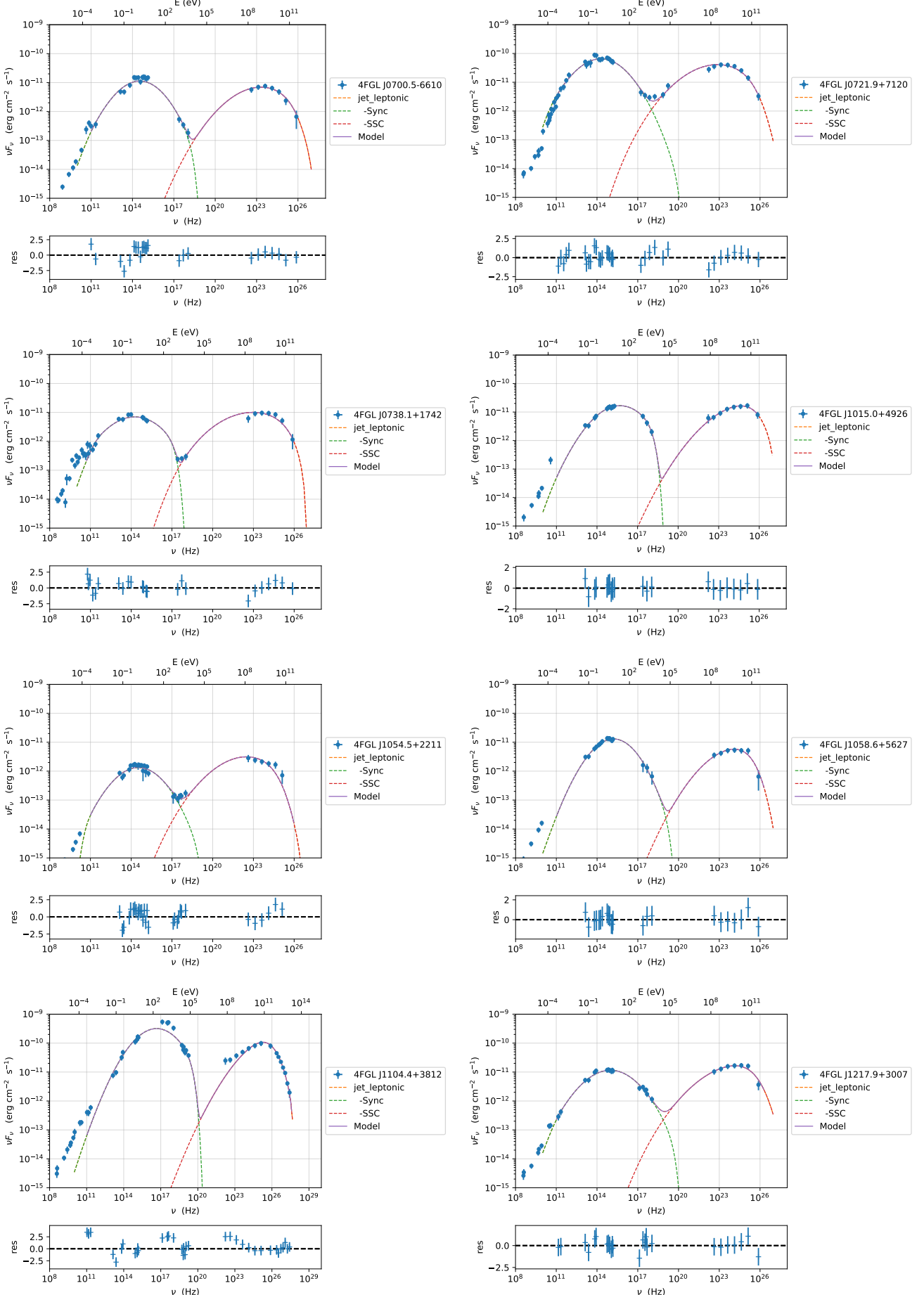


Figure 16 — continued.

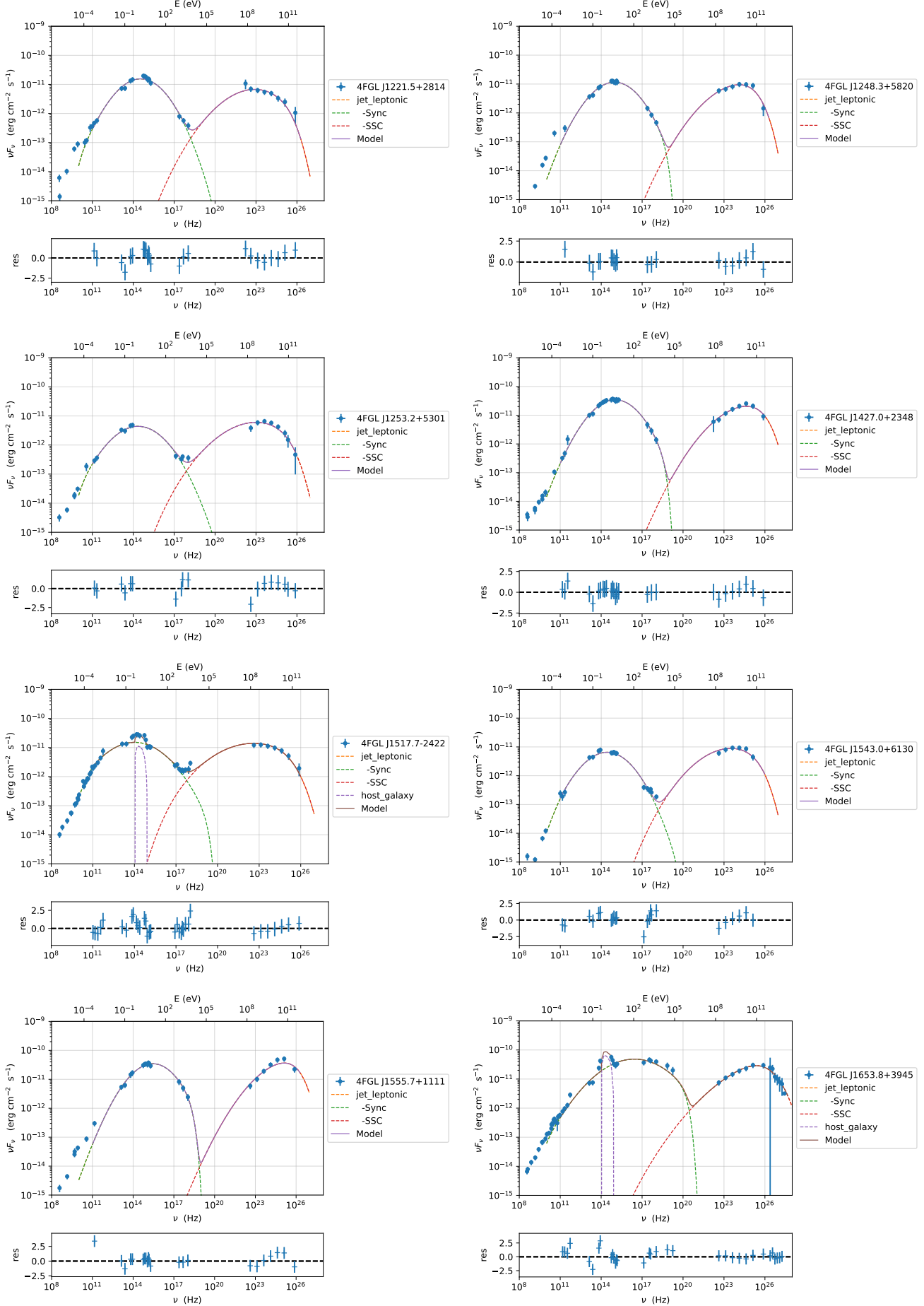


Figure 16 — continued.

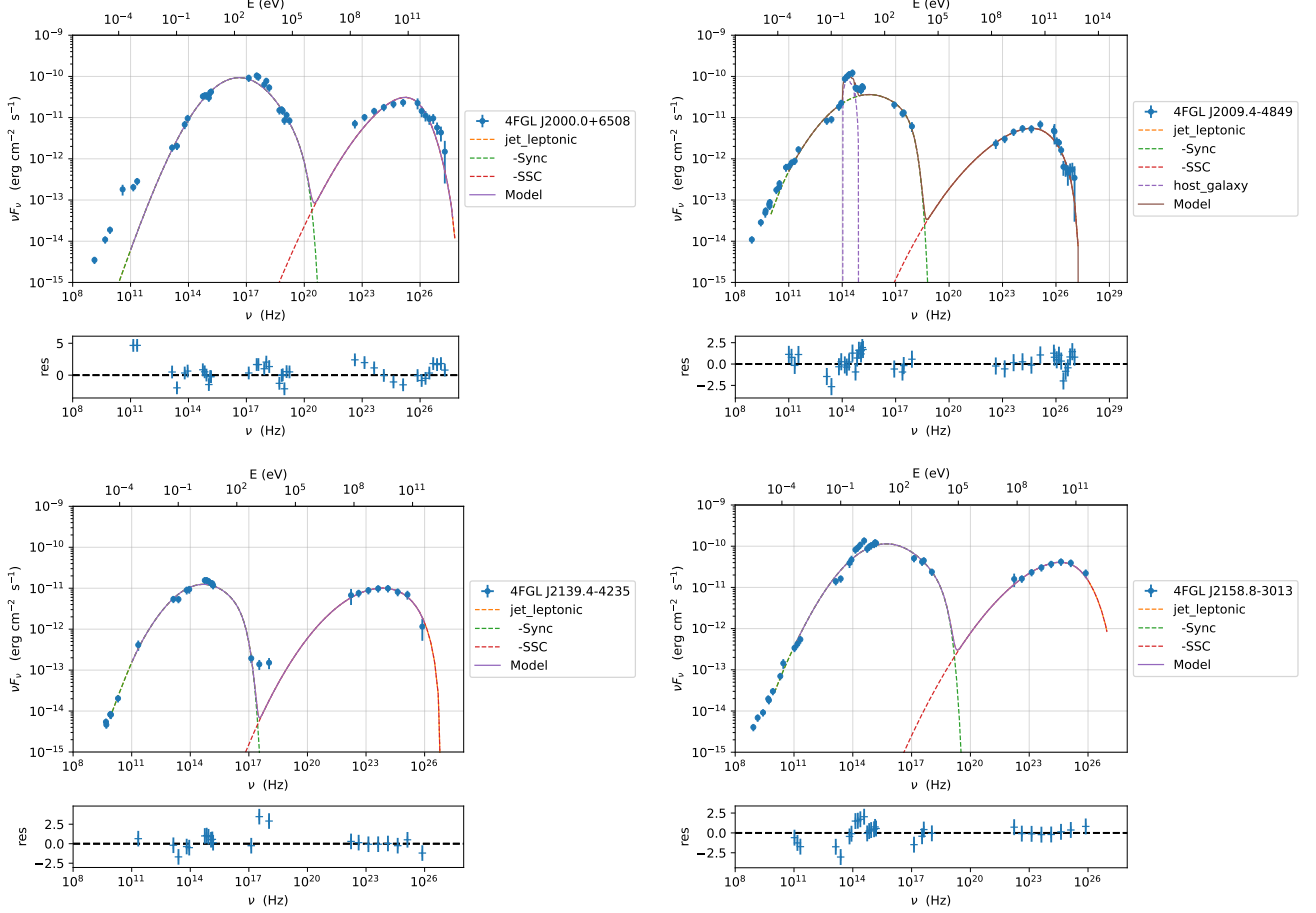


Figure 16 — continued.

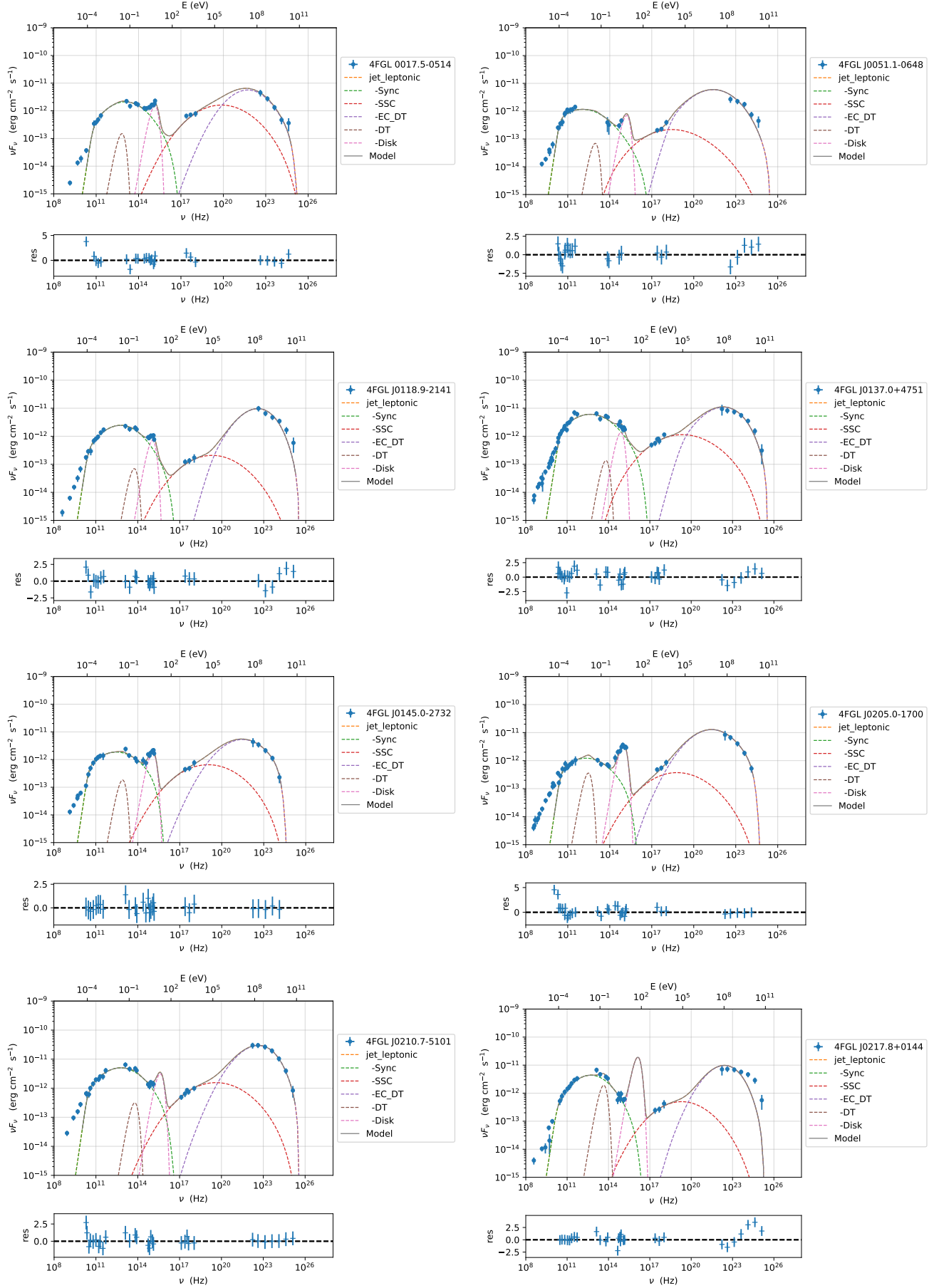


Figure 17. SED Modeling of EC Blazars.

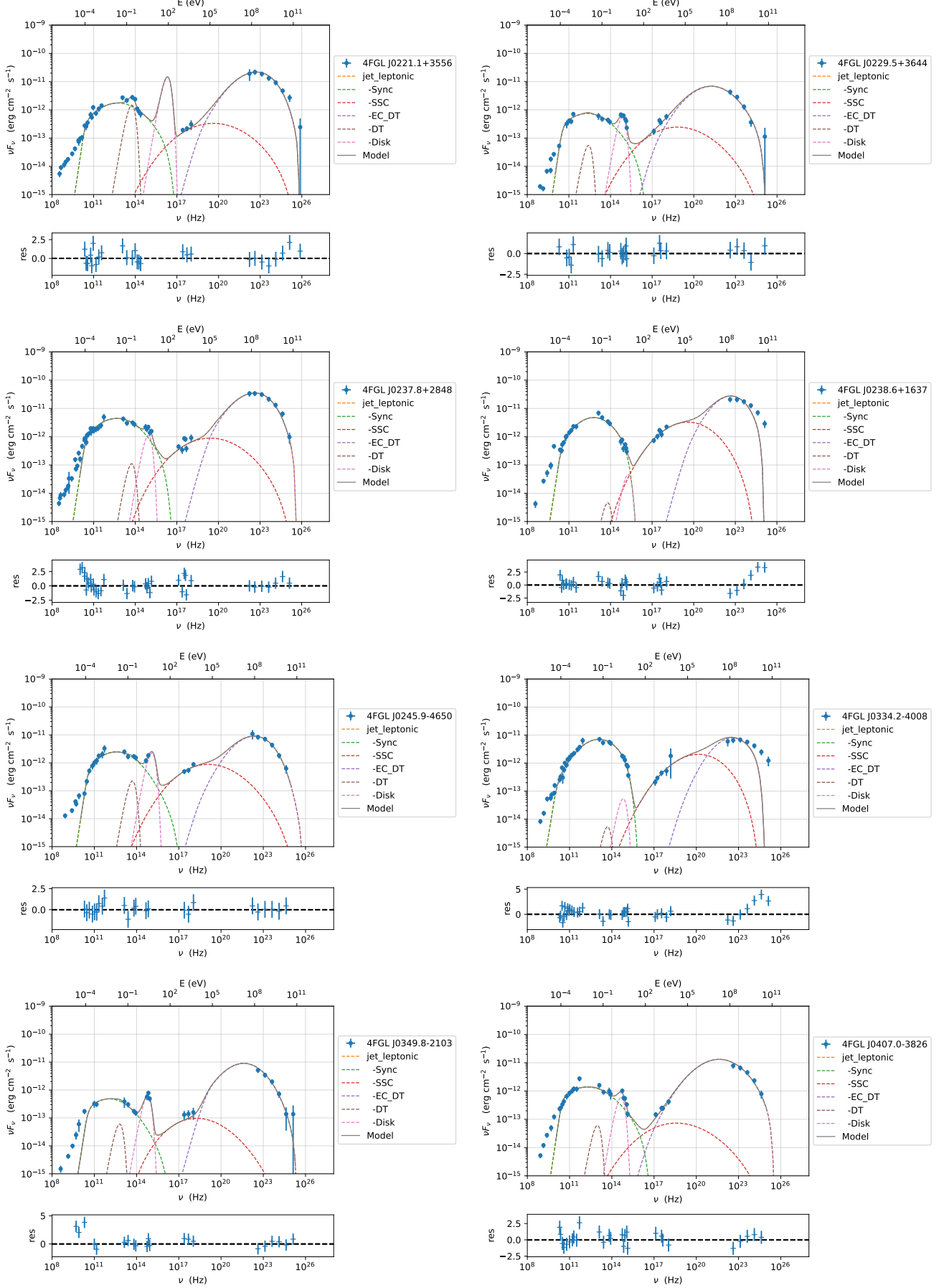


Figure 17 — continued.

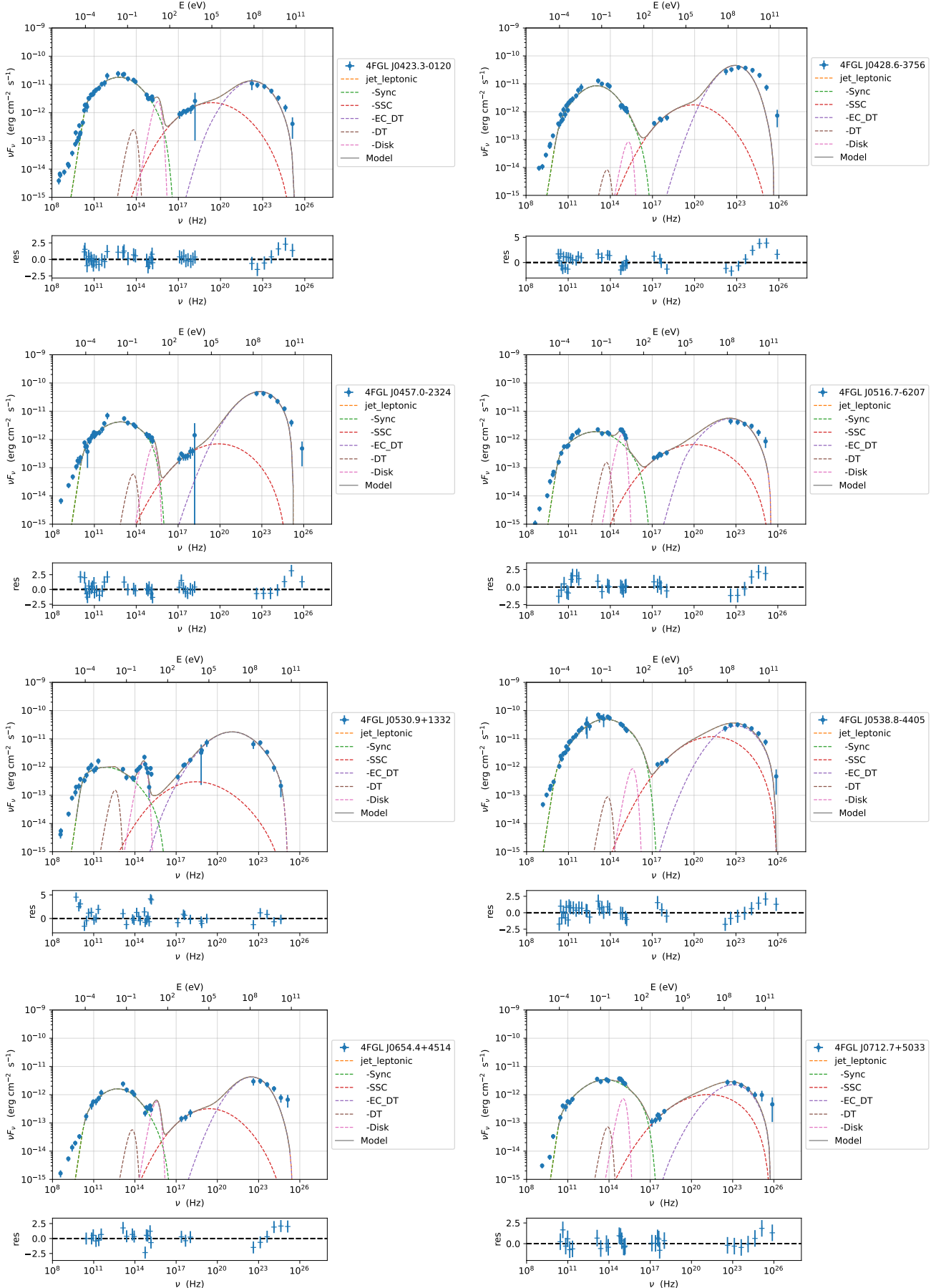


Figure 17 — continued.

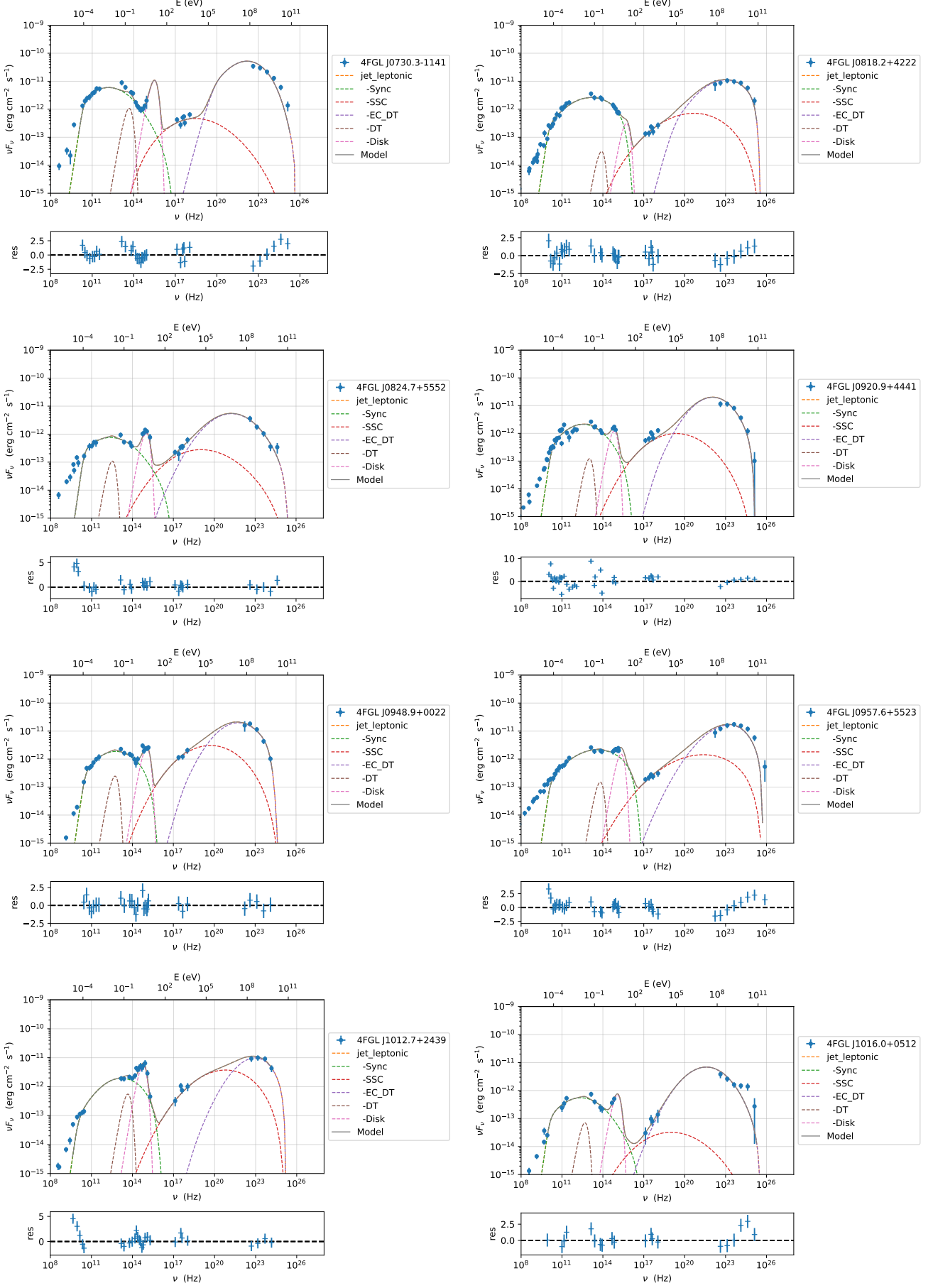


Figure 17 — continued.

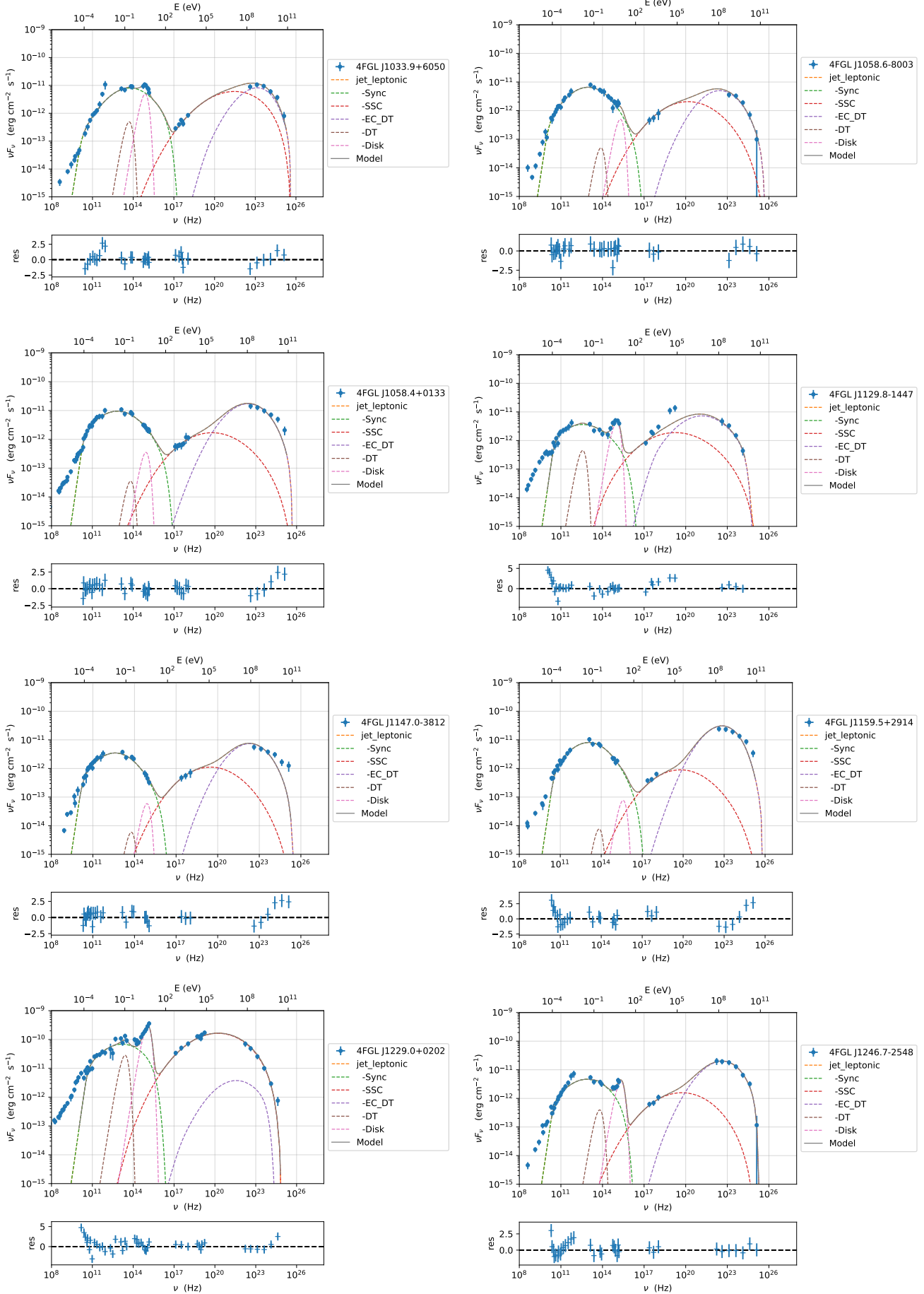


Figure 17 — continued.

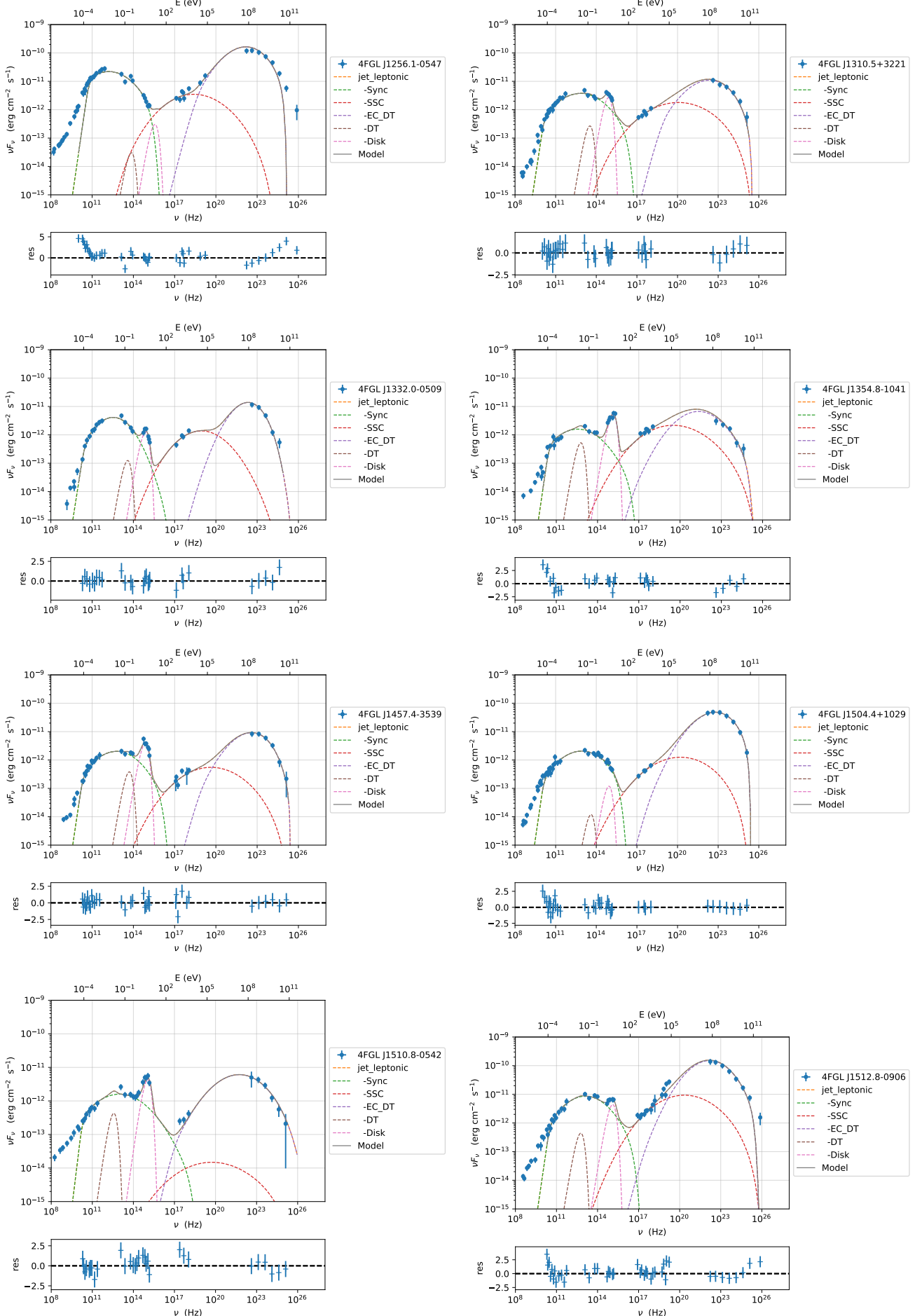


Figure 17. Spectral Energy Distribution (SED) for the eight pulsars.

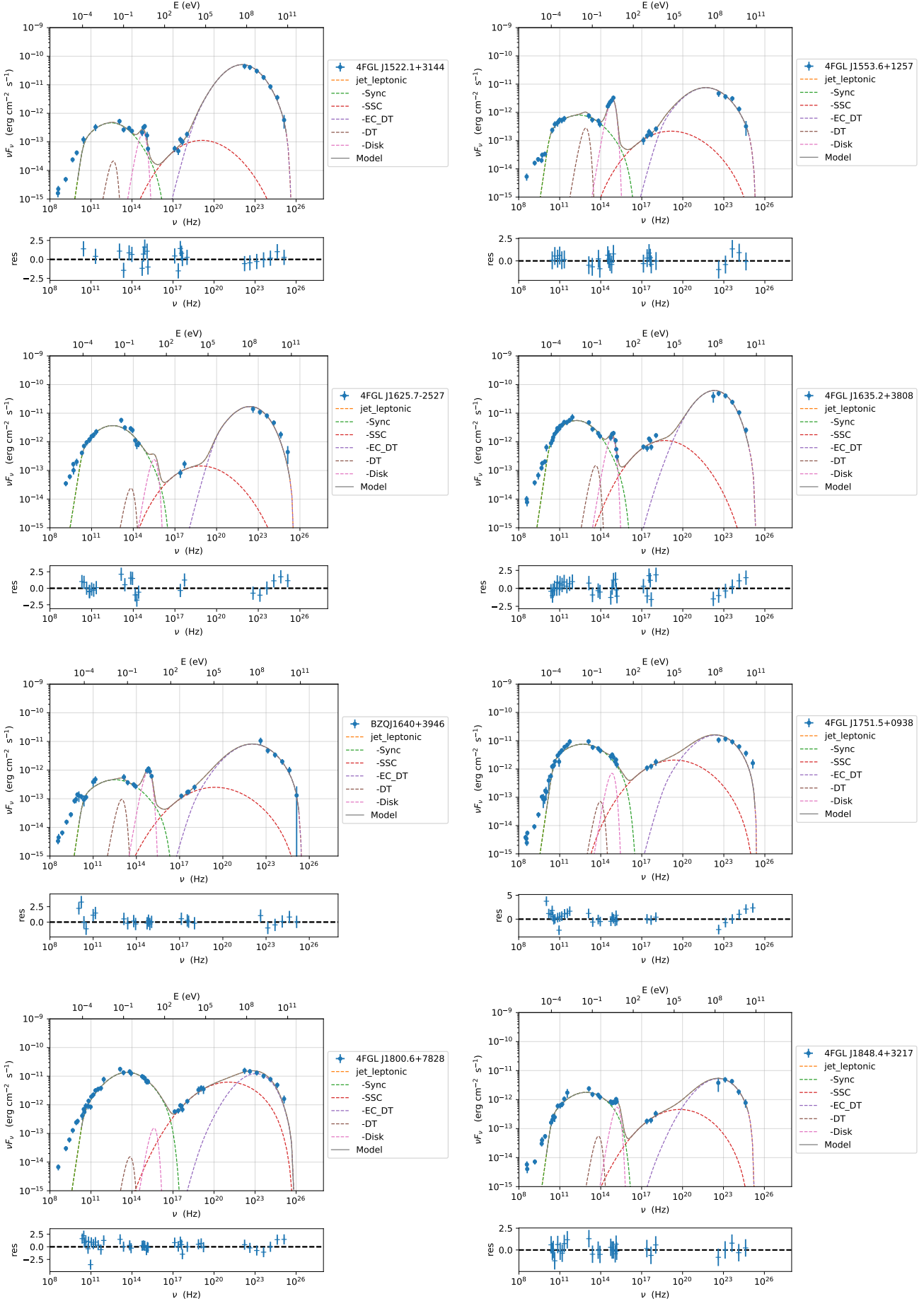


Figure 17 — continued.

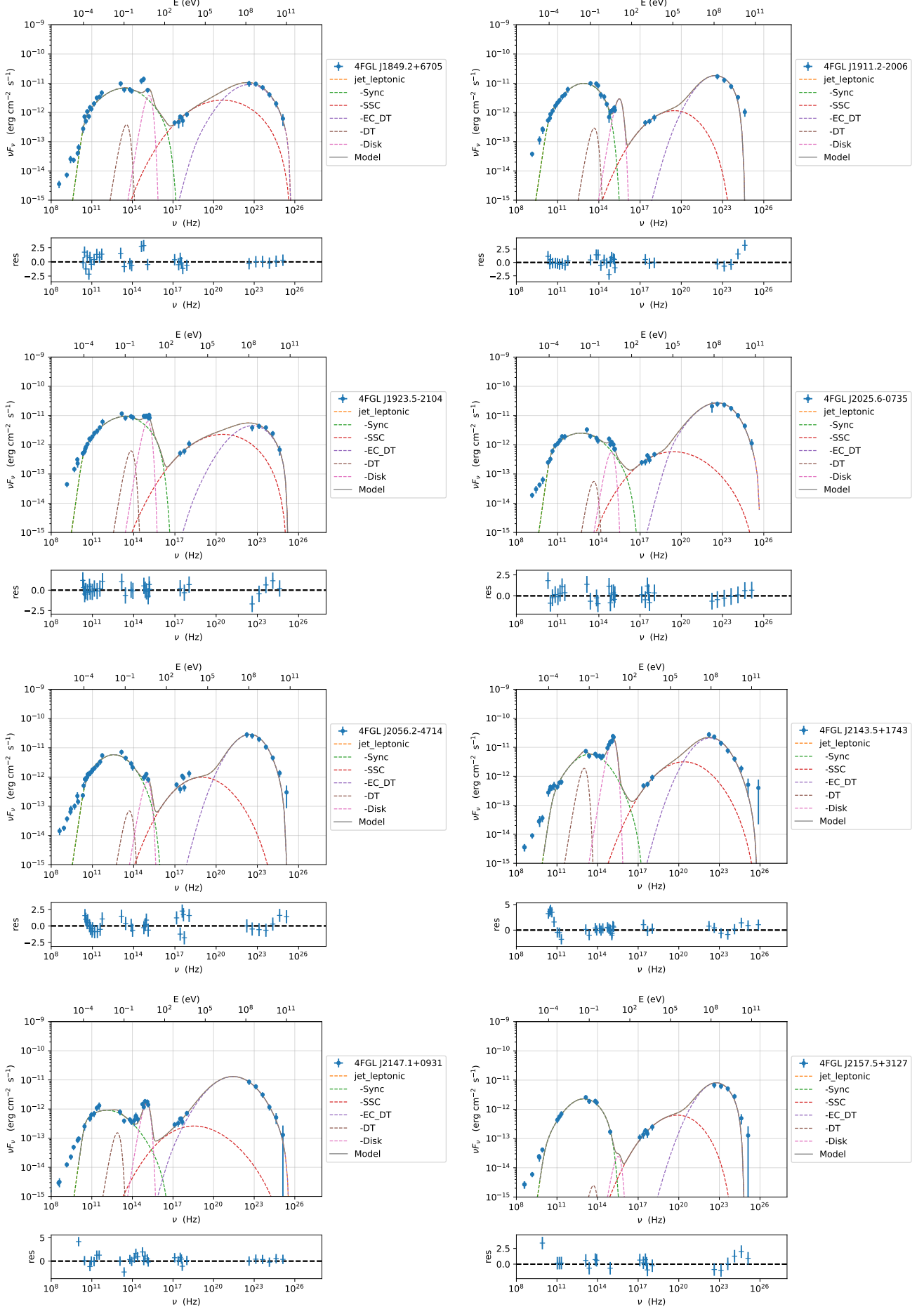


Figure 17 — continued.

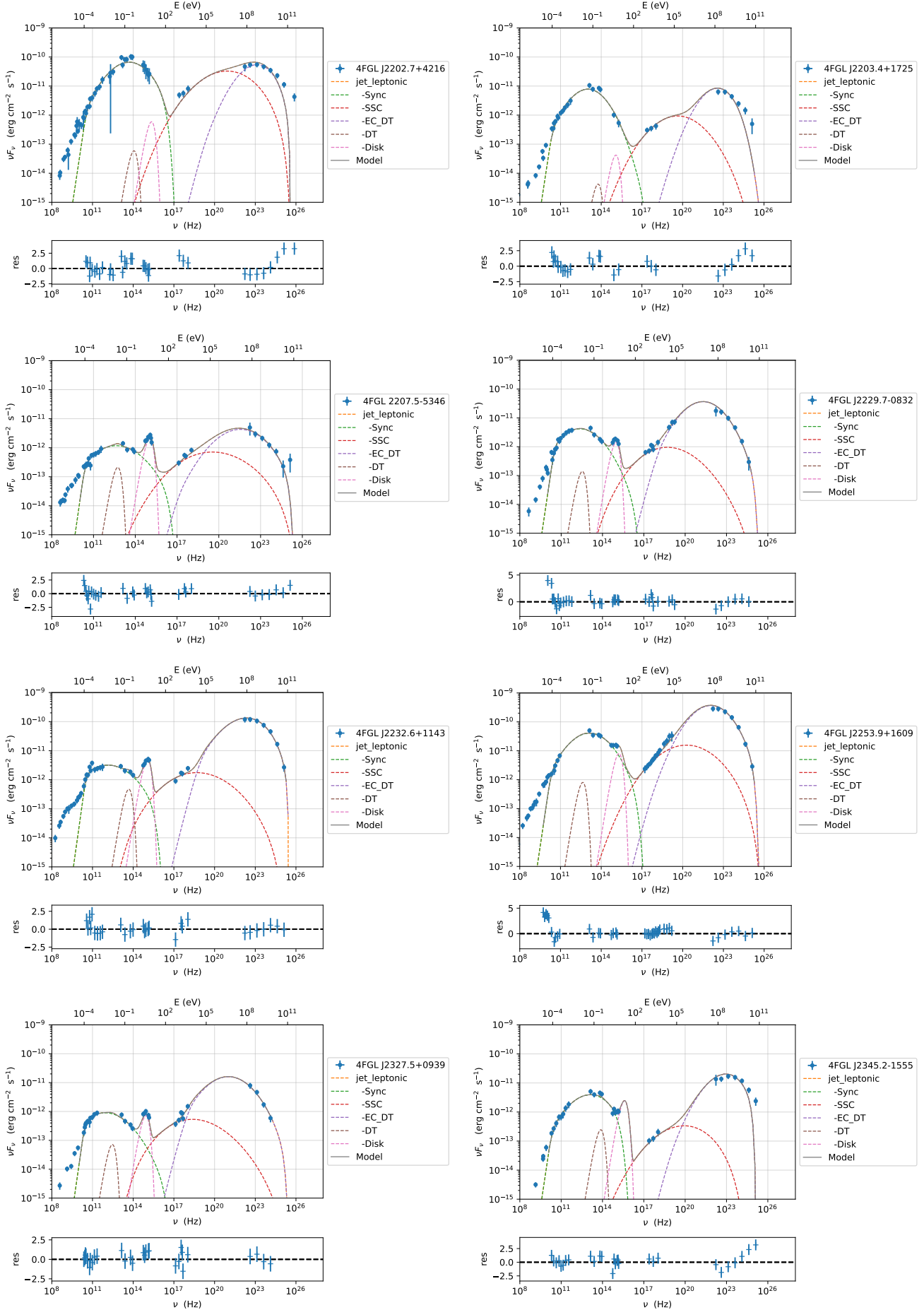


Figure 17 — continued.